



Does the syn- versus post-rift thickness ratio have an impact on the inversion-related structural style?

Alexandra Tamas^{1,2}, Dan M. Tamas^{1,2}, Gabor Tari³, Csaba Krezsek⁴, Alexandru Lapadat⁴, Zsolt Schleder³

¹Department of Geology, Babes-Bolyai University, Cluj-Napoca, 400084, Romania

5 ²Research Center for Integrated Geological Studies, Babes-Bolyai University, Cluj-Napoca, 400084, Romania

³OMV Energy, Vienna, 1020, Austria

⁴OMV Petrom, Bucharest, 013329, Romania

Correspondence to: Dan M. Tamas (danmircea.tamas@ubbcluj.ro)

Abstract. Many extensional basins worldwide are modified by subsequent compressional episodes, which lead to inverted
10 structures. The structures associated with the reactivation of preexisting faults play are critically important in forming suitable
subsurface traps for hydrocarbons. Major concerns regarding inverted structures are trap integrity and fault seal. In general,
the preferred structures have simple four-way closures as the result of only mild to moderate inversion.
Five physical sandbox models, coupled with Particle Image Velocimetry (PIV) analysis, have been performed to address the
influence of the syn- versus post-rift thickness ratio (Mode I and II) and the degree of positive inversion on the style of fault
15 propagation into and overall deformation of the post-rift cover. The results of these experiments are broadly comparable with
natural data examples from New Zealand, Israel and Turkey. The main control on the development of mild to moderate
inversion structures is the degree of inversion, and the style of deformation within the post-rift sequence appears to be different
due to the amount of displacement accommodated by the inherited listric fault and the thickness of the post-rift cover (Mode I
and II inverted structures). These observations do have a direct impact on the understanding of the geo-energy systems
20 associated with inverted structures.

1 Introduction

The concept of structural inversion is more than a century old (e.g. Lamplugh, 1919), however, the first generalised description
of inversion was offered by Bally (1984). Since then, the inversion tectonics plays an important role both in scientific research,
but more importantly for socio-economic purposes (see Zwaan et al., 2022, references therein).
25 To understand the structures and the factors controlling the structural style, inversion tectonics has been intensively studied in
outcrops (Krzywiec et al., 2009; Uzkeda et al., 2018; Dichiarante et al., 2021; Tamas et al., 2022a) interpreted in the subsurface
(Badley et al., 1989; Roberts, 1989; Krzywiec et al., 2009, 2018; Bosworth and Tari, 2021; Tamas et al., 2022b), modelled
physically and numerically (e.g. McClay, 1989, 1995; Buchanan and McClay, 1991; Mitra and Islam, 1994; Yamada and
McClay, 2003; Panien et al., 2005; Buiter et al., 2009; Bonini et al., 2012; Granado and Ruh, 2019; Zwaan et al., 2022 and
30 references therein).



The term “inversion” has a broad meaning in geoscience, in this study, we focus on positive structural inversion, which is defined by a basin which during its evolution has changed from subsidence to uplift (Harding, 1985). Hence the term inversion in this paper is referring exclusively to this type of inversion.

The structural styles associated with (positive) inversion are generally well-studied and understood and characterised by high angle out of graben thrusts, footwall shortcut thrusts, back-thrusts, forced folds or growth anticlines, among others (McClay and Buchanan, 1992).

Moreover, several factors controlling the structural style of basin inversion have been invoked which include: the strike and dip of the precursor faults (Gillcrust et al., 1987), preexisting extensional fault geometries (planar, listric, stepped; Gillcrust et al., 1987; McClay and Buchanan, 1992; Ferrer et al., 2017; Phillips et al., 2020); the architecture of the basin before inversion (Sieberer et al., 2023); the time interval since extension (e.g. Cooper and Warren, 2020), the amount of shortening relative to extension (e.g. Gillcrust et al., 1987; see also Mattioni et al., 2007 and references therein), the presence of salt/mechanical layering (e.g. Ferrer et al., 2016; Roma et al., 2018; Dooley and Hudec, 2020), syn-tectonic erosion and sedimentation.

In addition, Tari et al. (2020) observed a broad variation in the ratio between the thickness of the syn- versus post-rift successions in inverted structures and therefore suggested a subdivision of inversion tectonics into two modes. Mode I inversion structures are characterised by a thicker syn-rift succession than the post-rift sequence, and Mode II inversion occurs when the syn-rift strata is thinner than the post-rift one. The majority of modelling efforts to date addressed Mode I structures, even though there are numerous examples in nature where inversion occurred in Mode II (Tari et al., 2020).

The degree of inversion is important when discussing petroleum exploration. Based on numerous worldwide examples, the mild to moderate inversion structures are most preferred as petroleum exploration targets (Bevan and Moustafa, 2012). Their closures have a relatively small vertical amplitude, are simple in a map-view sense and well defined on reflection seismic data. These 4-way closures typically cluster above extensional depocenters which tend to contain source rocks that provide petroleum charge during and after inversion (MacGregor, 1995; Turner and Williams, 2004; Cooper and Warren, 2010, 2020; Bosworth and Tari, 2021). Strong to total inversion cases are generally not considered as ideal exploration prospects, mainly due to risk of breaching and also the associated seismic imaging challenges (Bevan and Moustafa, 2012). Migration also may pose a challenge due to structural complexity or the source rocks being uplifted above the hydrocarbon generation window (Tari et al. 2020, and references therein).

In this paper, we designed a set of analogue modelling experiments with original setups inspired by Ellis and McClay (1988) and Buchanan and McClay (1991) with the objective of improving our understanding regarding the control of syn- versus post-rift thickness ratios (Modes I and II proposed by Tari et al., 2020) as well as the degree of inversion on fault propagation into the post-rift cover and structural style exerted by inherited fault.



2 Methodology

2.1 Experiment design and working hypothesis

A series of **five analogue modelling experiments** were conducted to test the Mode I and Mode II inversion categories by Tari et al. (2020) (Fig. 1). Again, Mode I inversion is where the syn-rift succession, developed in the preexisting extensional basin unit, is thicker than its pre- and syn-inversion sequence part of the post-rift cover and Mode II inversion is with the opposite syn- versus post-rift succession ratio.

The experiments were conducted with an initial phase of extension followed by a shortening phase (positive inversion). The modelling rig and setup (Fig. 2a) were inspired by the setups of Ellis and McClay (1988) and Buchanan and McClay (1991) and consist of a fixed basement listric fault (footwall block) with a plastic sheet placed between the block and the (brittle only) modelling materials. The plastic sheet (Alkor foil) is mobile during extension (outward motion of the sidewall) because it is connected to the mobile wall. Prior to the compressional/inversion phase (inward motion of the wall), the plastic sheet is detached from the wall and fixed to a static part of the deformation rig, so that it would not become involved in hanging wall deformation during the contractional phase (Fig. 2a).

The fixed footwall (basement) block was 3D printed to be 10 cm deep and 20 cm wide with a listric geometry (cut-off angle of 60°), similar to that of Buchanan and McClay (1991). The deformation was driven by a stepper motor with an extension/compression rate of 5 mm/min. All the deformation was orthogonal and there are no lateral variations of the setup or materials within the models. The models were 20 cm wide and their initial length was calculated to reach the same value (41.5 cm) prior to inversion (Fig. 2).

2.2 Materials, scaling and monitoring

The model layering is brittle-only and is made out of dry, coloured, cohesionless quartz sand with an average grain size of 0.19 mm (Fig. 2b). Dry quartz sand has been proven as a suitable material and has often been used to model brittle inversion tectonics (e.g. Koopman et al., 1987; Buchanan and McClay, 1991; McClay and Buchanan, 1992; Yamada and McClay, 2004; Gomez et al., 2012; Molnar and Buitert, 2022). For a more detailed review of inversion model setups and materials, see Zwaan et al. (2022). The models were constructed from alternating layers of yellow (light brown) and coloured sand that were sieved into the apparatus and scraped to the desired thickness. Pre-rift strata consisted of alternating blue-yellow sand layers, whereas syn-extensional strata were green-yellow sand layers. A thin layer of black sand was sieved between each coloured layer in order to increase contrast and facilitate interpretation. At the end extension, an alternating sequence of black-yellow sand was added. No syn-kinematic layers were added during inversion.

The length scaling ratio of the models to natural structures is approximately 10⁻⁵, thus, 1 cm in the model scales to approximately 1 km in nature (Ellis and McClay, 1988; Buchanan and McClay, 1991; Yamada and McClay, 2004).

Deformation within the models was recorded by several techniques. The surface (top-view) strain was recorded by timelapse photography taken with two DSLR cameras placed at an angle to the top of the experiment. These photos were later processed



in StrainMaster (laVision) to perform 3D Particle Image Velocimetry (PIV), which is a 3D digital image correlation technique used to extract information regarding, i.e. total or incremental shortening, velocity, displacement vectors, strain, etc. (e.g. Adam et al. 2005).

The temperature and humidity laboratory conditions are maintained constant ($23^{\circ}\text{C}\pm 3$, $45\%\pm 5$).

At the final stage of the experiments, the models were wetted and consolidated with a 10% gelatine/water solution. Serial vertical sections were cut every 2 cm, photographed and interpreted.

2.3 Experimental limitations

One of the limitations of the analogue modelling experiments is represented by the edge effects generated by the friction with the side walls, effects visible on the top-view PIV data. These effects were reduced, but not eliminated, by coating the walls with a hydrophobic silicone polymer (Rain-X) (Cubas et al. 2013; Tamas et al. 2020). The sections on which the results of this paper were based are further away from the side walls (at least 4 cm).

Determining the presence of faults in small offset areas within the models was sometimes difficult because the faults are not always represented by a single shear plane but by a series of shear bands / shear zones. This is due to the relatively large grain size of the modelling materials as compared to nature.

3 Analogue modelling results

All of the experiments described in this paper start with the same pre-extensional setup, consisting of a 10 cm thick stack of coloured sand layers (yellow-blue) in the hangingwall of a major listric fault (Fig. 2c and d). The applied extension is 2.5 cm in experiments 3 and 5, 4.5 cm in experiments 1 and 2, and 9 cm in experiment 4 (Fig. 2d). Thus, the description of the development of the extensional geometries will be similar as we have only three different extensional setups. All of the experiments were designed in such a way that the pre-inversion length of the experiments is the same, respectively 41.5 cm (Fig. 2d). The results of such extensional setups and the development of such geometries have been described in great detail by other authors (e.g. Ellis and McClay, 1988; McClay, 1989; Yamada and McClay, 2004) and are not the main focus of this paper. The focus area will be the inversion part of the experiments, where the first four experiments describe a different syn- vs post-rift thickness ratio setup, and in the case of experiment 5, a different amount of total inversion is applied.

3.1 Experiment 1

This experiment (Fig. 3) consisted of an extensional part with 4.5 cm total extension with the addition of successive growth layers of sand (green-yellow) every 1.5 cm of extension. The maximum thickness of the growth strata is 4.4 cm at the end of extension (Fig. 2c and d). PIV monitoring was used to visualise and interpret the cumulative strain patterns between subsequent phases of extension (Fig. 3a-c) and will be described below.



In the first phase of extension, the deformation started with the development of a roll-over anticline and block rotation. This led to areas with diffuse extensional strain forming in the area separating the non-rotational zone of the hangingwall from the zone of predominant rotation (above the listric fault) (Fig. 3a). During the second stage of extension with an additional 1.5 cm of extension, the areas of diffuse extensional strain become more localised (Fig. 3b). The first faults bounding the crestal collapse graben start to develop, most of them being antithetic faults.

At the end of the third extensional phase, with further 1.5 cm of extension, very clear areas of localised extension could be identified on the PIV data (Fig. 3c). In addition, several clear antithetic faults are visible on the top view of the experiment (Fig. 3d). After inverting and cutting the experiment more antithetic and synthetic faults were later identified in cross-section, mainly localised in the crestal collapse block (Fig. 3g and h). However, the total amount of applied extension did not lead to the formation of major fault systems (Fig. 3d and g).

After the extension, a 2.2 cm thick post-rift succession of sand layers (black-yellow) was added on top of the experiment (Fig. 2). This represents half the thickness of the syn-rift sand added during extension.

To achieve inversion, the extended model was now exposed to 1.7 cm of horizontal compression. This compression led to the inversion of the listric fault and the development of several small footwall shortcut splay thrust faults in the post-rift sediments (Fig. 3e-h). The main reverse fault extends throughout the post-tectonic cover and just reaches the surface forming a well-defined hangingwall anticline (Fig. 3f-h), while the frontal splay faults tip within the post-rift stratigraphy just above the second black layer (Fig. 3g). Except for the main listric fault, no visible reactivation was identified in any of the syn- and antithetic normal faults in cross-section. Some localised areas of compressional strain above the preexisting minor extensional faults are visible on the PIV map (Fig. 3e; in teal). These zones are wider, and the strain is more diffuse than the one associated with the inverted listric fault however, they could indicate a minor inversion of the preexisting minor extensional faults.

3.2 Experiment 2

This experiment (Fig. 4) consisted of 4.5 cm total extension with the addition of successive growth layers of sand (green-yellow) every 1.5 cm of extension. The extension part of this experiment is identical to Experiment 1, hence, the experiment develops in a very similar manner. In the first phase of extension, the deformation started with the development of a roll-over anticline and block rotation, which led to areas with diffuse extensional strain (Fig. 4a). These zones become more localised with additional extension (Fig. 4b and c). At the end of the extensional stage, apart from the listric fault several small antithetic faults can be observed localised in the crestal collapse block both in map-view (Fig. 4d) and in cross-section after inverting and cutting the experiment (Fig. 4g and h).

After the extension, a 4.4 cm thick post-rift succession of sand layers (black-yellow) was added on top of the experiment (Fig. 2c and d). This represents the same thickness as the syn-rift sand added during extension.

Similar to Experiment 1, a 1.7 cm of horizontal compression was applied to the extended model. This compression led to the inversion of the listric fault and the development of a small splay fault in the post-rift sediments (Fig. 4e-h). In this case, the main reverse fault only seems to extend halfway through the post-tectonic cover and tip within the third black layer, without



155 reaching the surface (Fig. 4g). Above the reverse fault the layers are, the surface expression of this structure is characterised by minor bulging (Fig. 4f-h) which is barely visible in top-view (Fig. 4f). Like Experiment 1, only the main listric fault was reactivated and no visible reactivation was identified in any of the syn- and antithetic normal faults in cross-section. On the PIV map, a wide zone (c. 1 cm wide) of compressional strain formed above the inverted listric fault (in green), while above the preexisting extensional faults only a diffuse zone of compressional strain is visible (Fig. 4e).

160 3.3 Experiment 3

This experiment (Fig. 5) consists of 2.5 cm total extension with the addition of successive growth layers of sand (green-yellow) every 1.25 cm of extension. The maximum thickness of the growth strata is 2.2 cm at the end of extension (Fig. 2c and d).

Similar to Experiments 1 and 2, in the first phase of extension, the deformation started with the development of a roll-over anticline and block rotation, which led to areas with diffuse extensional strain. These zones become more localised with
 165 additional 1.25 cm of extension (Fig. 5a). These small total amounts of applied extension did not lead to the formation of major faults systems and apart from the listric normal fault only a minor antithetic fault is visible in cross-section after inverting and cutting the experiment (Fig. 5e and f).

After the extension, a 4.4 cm thick post-rift succession of sand layers (black-yellow) was added on top of the experiment (Fig. 2). This represents double the thickness of the syn-rift sand added during extension (2.2 cm).

170 Following the addition of the post-rift sequence, we applied 1.7 cm of horizontal compression to invert the model. This compression led to the inversion of the listric fault and the development of small splay thrust faults in the post-rift sediments (Fig. 5e and f). Similar to Experiment 2, the main reverse fault only seems to extend halfway through the post-tectonic cover and tip within the third black layer, without reaching the surface (Fig. 5e and f). At surface, only minor bulging can be observed, which is barely visible in the top-view (Fig. 5d). On the PIV map, a wide zone (c. 1-1.5 cm) of compressional strain formed
 175 above the inverted listric fault (in green), while away from the listric fault only a diffuse zone of compressional strain is visible (Fig. 5c).

3.4 Experiment 4

This experiment (Fig. 6) consists of 9 cm total extension with the addition of successive growth layers of sand (green-yellow) every 1.5 cm of extension. The maximum thickness of the growth strata is 8.8 cm at the end of extension (Fig. 2c and d).

180 The first 4.5 cm of extension of this experiment evolves similarly to Experiments 1 and 2. The deformation started with the development of a roll-over anticline and block rotation, which led to areas with diffuse extensional strain. These zones become more localised with an additional 1.5 cm of extension (Fig. 6a). During the third and fourth stages of extension with additional 3 cm of extension, the areas of extensional strain become more numerous and localised (Fig. 6b). As the extension is continued with further two steps of 1.5 cm each of extension, very clear areas of localised extension could be identified on the PIV data
 185 (Fig. 6c). Also, numerous clear synthetic and antithetic faults are visible on the top view of the experiment (Fig. 6d). After inverting and cutting the experiment more antithetic and synthetic faults were later identified in cross-section, mainly localised



in the crestal collapse block (Fig. 6g and h). Compared with the previous experiment, this 9 cm of total extension led to the formation of more significant fault systems (Fig. 6g and h).

After the extension, a 4.4 cm thick post-rift succession of sand layers (black-yellow) was added on top of the experiment (Fig. 2). This represents half the thickness of the syn-rift sand added during extension.

Similar to Experiment 1-3, to achieve inversion, the extended model was exposed to 1.7 cm of horizontal compression. This compression led to the inversion and propagation of the reverse fault halfway through the post-rift sediments (Fig. 6e-h). Except for the main listric fault, no visible reactivation was identified in any of the syn- and antithetic normal faults in cross-section or top-view (Fig. 6f-h). Some localised areas of compressional strain above the preexisting minor extensional faults is visible on the PIV map (Fig. 6e; in teal). These zones are wide and diffuse however, they could indicate a minor inversion of the preexisting minor extensional faults.

3.5 Experiment 5

This experiment (Fig. 7) consisted of 2.5 cm total extension with the addition of successive growth layers of sand (green-yellow) every 1.25 cm of extension. The maximum thickness of the growth strata is 2.2 cm at the end of extension (Fig. 2).

Similar to Experiment 3, in the first phase of extension, the deformation started with the development of a roll-over anticline and block rotation, which led to areas with diffuse extensional strain. These zones become more localised with additional 1.25 cm of extension (Fig. 6a). These small total amounts of applied extension did not lead to the formation of major faults systems and apart from the listric normal fault with only a minor antithetic fault visible in cross-section after inverting and cutting the experiment (Fig. 5e and f).

After the extension, a 4.4 cm thick post-rift succession of sand layers (black-yellow) was added on top of the experiment (Fig. 2). This represents double the thickness of the syn-rift sand added during extension (2.2 cm).

Following the addition of the post-rift sequence, we applied 2.5 cm of horizontal compression to invert the model. This compression led to the inversion of the listric fault, which extended throughout the post-tectonic cover and reached the surface forming a well-defined hangingwall anticline (Fig. 7e and f). As the thrust fault accommodated more displacement compared with previous experiments, the thrust fault is clearly visible at the surface (Fig. 7d), while the PIV map is characterised by a well-defined, narrow zone of compressional strain (Fig. 7c; in green). Away from the listric fault, only a diffuse zone of compressional strain is visible (Fig. 7c; in blue), as well as a diffuse zone of extensional strain (Fig. 7c; in yellow) which can indicate minor extension in the crest of the anticline

4 Discussions and examples from nature

In the following sections, we summarise the experimental results (Fig. 8) in the context of the Mode I/Mode II inversion structures (Tari et al., 2020) and then compare them with natural examples with implications for surface and subsurface interpretation.



4.1 Summary of model results

We present five experiments, of which all had the same geometry of listric fault block and 10 cm of pre-kinematic layers (Fig. 2c and d).

From extension point of view, Experiments 3 and 5 are similar and experienced 2.5 cm of extension. This led to a maximum thickness 2.2 cm of growth strata accommodated in the hangingwall of the listric fault and the development of a minor antithetic fault with submillimetre displacement (Fig. 8).

Experiments 1 and 2 experienced 4.5 cm of extension, which led to a maximum thickness 4.4 cm of growth strata accommodated in the hangingwall of the listric fault and the development of 5-6 minor antithetic and synthetic faults with minor displacements (Fig. 8).

Experiment 4 had the most displacement (9 cm), which led to the development of numerous (c. 9-10 faults) minor antithetic and synthetic faults (Fig. 8).

After extension, Experiment 1 was covered by 2.2 cm of post-tectonic cover, while Experiments 2 to 5 had 4.4 cm thick post-rift.

The inversion amount for Experiments 1 to 4 was 1.7 cm, which led to the propagation of the reverse fault just near the surface for Experiment 1, which only had 2.2 cm of post-tectonic cover. However, for Experiments 1 to 3, which had 4.4 cm of post-tectonic cover, the reverse fault propagated only halfway through the post-tectonic cover (Fig. 8). Experiment 5 experienced 2.5 cm of inversion, which led to the propagation of the inverted fault through the entire 4.4 cm of post-tectonic cover and forming well-defined thrust fault (Fig. 8). For all experiments (1 to 5) the final, inverted geometry shows that the post-kinematic unit is, though slightly, but almost uniformly uplifted above its footwall's regional elevation. There is a slightly more pronounced uplift above the concave segment of the listric fault, which is most evident in Experiment 5, where the reverse slip is the largest. The reason for this uniform uplift above the footwall regional is the horizontal compaction and related thickening of the whole sand pack ahead of the left-ward moving backstop that facilitates the reverse slip.

According to Mode I/Mode II classification of Tari et al. (2020), Experiments 1 and 4 have the post-rift cover half of the syn-rift (Mode I), Experiment 2 have the post-rift equal to syn-rift, while Experiments 3 and 5 have post-rift cover double than the syn-rift (Mode II) (Figs 2c, d and 8).

In order to answer the question if the inversion-related structures are influenced by the syn- to pots-rift ratios, we can first compare Experiments 1 and 4, both having a Mode I setup. The inversion structures in Experiment 1 can be characterised as reverse-fault-bounded (Tari et al. 2020), which are considered typical for Mode I (Fig. 1). However, in the case of Experiment 4, the structures that develop in the uppermost layers of the post-rift sequence is characterised by gentle folds which is a typical Mode II structure (Fig. 1).

If we look further at Experiments 2, 3 and 4, they all show similar inversion-related structures. The contractionally reactivated listric fault does not propagate through the entire post-rift sequence but stops somewhere mid-section and forms a gentle



250 anticline in the uppermost layers regardless of the syn-rift to post-rift ratios. Note that Experiment 2 has the post-rift cover equal to the syn-rift, Experiment 3 has a Mode II setup, while Experiment 4 had a Mode I setup.

Nonetheless, it is clear if we compare Experiments 3 and 5, which both have a Mode II setup and an identical extension amount and syn-tectonic cover thickness, that the inversion-related structures are different (Fig. 8). This is because the inversion amounts in Experiment 3 is 1.7 cm compared to 2.5 cm in Experiment 5.

255 Based on our experiments observations, we suggest that the syn- to post-rift ratios do not seem to have the primary influence of the inversion-related structures, the degree of inversion does. The structural style shows that the style and propagation of contractional structures are mostly affected by the amount of displacement accommodated by the inherited listric fault and the thickness of the post-rift cover.

Apart from the inversion of the listric fault, no inversion of the antithetic or synthetic crestal collapse graben faults (e.g. 260 Gillcrist et al., 1987; Buchanan and McClay, 1991) is visible in our experiments in cross-sections. However, the PIV-analysis shows localised areas of compression which can indicate mild reactivation of the crestal collapse graben faults, which are below the visible scale of the experiment. This also highlights the need to improve the ‘resolution’ limitations of analogue models and use it as a direct example to understand the subsurface structures which are below the seismic resolution.

4.2 Examples from nature

265 The examples in this section were gathered from specific case studies where inversion structures with petroleum traps developed in Mode II inversion.

4.2.1 Taranaki Basin, New Zealand

The Taranaki Basin is considered a classic location for inverted structures (Nicol et al., 2007; Giba et al., 2010; Reilly et al., 2017). This basin saw continental rifting during the Senonian when several half-graben systems developed. Rifting was 270 replaced by a passive margin stage spanning the entire Paleogene. During the early Miocene prominent elongated anticlinal structures were formed due to positive inversion. Two of these are reproduced here using a reflection seismic section (Fig. 9b) from a 3D seismic data set (Wunderlich et al., 2019; Wunderlich and Mayer, 2019). The stratigraphy within these structures is very well constrained due to the numerous hydrocarbon exploration wells. These wells delineated two gas-oil fields, Manaia and Maari, trapped in 4-way robust closures along the crests of these inversion structures (Fig. 9a) with reservoirs and source 275 rocks drilled at multiple levels. Note that the Maui-4 well even reached the pre-rift basement by penetrating the entire post-rift and syn-rift succession (Fig. 9b).

The wedge-shaped Upper Cretaceous units with a growth element associated with the master faults display the early extensional stage of these faults. There is no growth pattern associated with the Paleogene sequence as it is already the post-rift sequence associated with the thermal subsidence on a passive margin. However, the pre-T85 (i.e. pre-Upper Miocene) 280 sequence was folded into slightly asymmetric anticlines during the late Miocene between about 10-7.6 Ma ago. Importantly,



the master faults did not propagate up and offset the thick post-rift basin fill (Fig. 9b) even though the reverse movement on the master faults restored entirely the former extensional offset on the Manaia fault and even more on the Maari structure. Since the post-rift basin fill is about twice as thick as the syn-rift fill in these structures, they are both Mode II inversion structures sensu Tari et al. (2020). There is evidence for the slight reactivation of positive inversion after the formation of the major angular unconformity postdating the bulk of the deformation, but it contributed very little to the structural relief (Fig. 9). Neither of the master faults propagated through the entire post-rift succession, therefore, both structures manifest themselves as buckle folds with a subtle asymmetry observable in the geometry of the post-T70 sediments. The lack of fault breakthrough across the entire sedimentary sequence is significant as the inversion-related vertical reverse movement was quite substantial, on the order of 600-800 m, given the offset seen on the T10 seismic marker (Fig. 9b).

We suggest that the trishear model of Erslev (1991) is applicable to the western limb of the Manaia anticline. Trishear folding takes place entirely ahead of the propagating fault tip, with a waning fault slip by folding within a triangular zone, the apex of which is pinned to the fault tip (Fig. 9). Trishear modelling of fold-fault geometries can be used to test the validity of trishear folding (Hardy and Ford, 1997; Allmendinger, 1998), which we have not done yet. At any rate, none of our physical experiments (Figs. 2-8) did reproduce the observed geometry seen on the seismic profile so far, which we attribute to the effect of a very thick post-rift sedimentary cover absorbing the contractional deformation over the reverse master fault which tipped out relatively deep in the core of the structure (Fig. 9b).

4.2.2 Eastern Mediterranean, Israel

The broader Levant area in the Eastern Mediterranean is also considered as a classic area for inversion tectonics (Walley, 1998; Bosworth et al., 1999). There are a large number of structures, both offshore and onshore in Egypt (Bevan and Moustafa, 2012; Moustafa, 2010, 2019; Bosworth and Tari., 2021) and in Israel (Gardosh et al., 2010; Gardosh and Tannenbaum, 2014; Needham et al., 2017) which have been well documented and provide useful exploration templates for analogue structures elsewhere (see Tari et al., 2020, for an overview).

The very large gas fields discovered in the deepwater Levant in the last two decades are all but one (Zohr) trapped in inverted structures. These traps manifest themselves as slightly asymmetric buckle folds in the post-rift strata high above the underlying syn-rift grabens. As to the post- to syn-rift ratios in these structures, they all tend to be developed in Mode II inversion, i.e. Tamar with 2:1 and Leviathan with about 1.5:1 (Tari et al., 2020). Importantly, at the level of the gas discoveries high in the apex of these anticlines there are no faults present which would correspond to the upward propagation of the syn-rift boundary faults from beneath (Needham et al., 2017). Clearly, the reverse faulting caused by the inversion could not break through the uppermost 2-3 km thick part of the post-rift succession (Roberts and Peace, 2007), but instead, the basin fill deformed into large open folds.

Here we reproduce just one additional data example from the Israeli sector of the Eastern Mediterranean (Fig. 10). The outboard Yam West anticline has a post-to syn-rift ratio of about 4:1 and the inboard Yam anticline has an even larger number if the cross-section could be considered very precise at the depth of 7-8 km. However, there are no wells penetrating the very deep



Permo-Triassic sequence in this part of the offshore Levant, and the cross-section is relying only on seismic interpretation at this depth (Gardosh et al., 2010; Gardosh and Tannenbaum, 2014). Regardless, these features formed, like all other Syrian Arc anticlines in the offshore, by Mode II inversion. The faults, in this case, were interpreted to propagate across the entire post-rift sequence of the inversion structures (Fig. 10).

4.2.3 Black Sea, Turkey

There are many hydrocarbon fields in the Black Sea associated with inversion-related structures (see Bosworth and Tari, 2021, for an overview). In the Histria Trough of Romania, multiple phases of Cenozoic inversion have been described (Dinu et al., 2005; Munteanu et al., 2011; Krezsek et al., 2018). Golitsyna structure, the first offshore discovery in the Gulf of Odessa (Ukraine), is an inversion-related anticline with Paleocene chalk and Oligocene sandstone reservoirs (Robinson et al., 1995; Robinson and Kerusov, 1997; Khriachtchevskaia et al., 2009, 2010; Stovba et al., 2020).

In the Turkish sector, the biogenic gas field of Akcakoca was discovered by Turkish Petroleum in 1976 (Fig. 11). Subsequent drilling proved the commerciality of this gas find with an inverted anticlinal trap for this field (Robinson et al., 1995; Alaygut et al., 2004; Menlikli et al., 2009). The same late Eocene regional shortening episodes which caused inversion on the conjugate Ukrainian side of the Black Sea formed several anticlinal structures along the Pontides both offshore and onshore (Menlikli et al., 2009; Okay et al., 2018; Tüysüz, 2018). The regional collision-related shortening at the end of the Lutetian caused uplift, basinward tilt and severe truncation of the entire margin (Okay et al., 2018).

To illustrate the Eocene inversion in the central part of the Turkish Black Sea region, we reproduced a seismic section across the Akcakoca Field (Fig. 11a) by Korucu et al. (2013). Additional seismic examples of the Akcakoca structure were published by Robinson et al. (1995) and Önal and Demirbağ (2019). The Akcakoca anticlinal trend is the outboard one among a few other inverted anticlines striking E-W to WNW-ESE in the offshore.

The major reverse fault controlling the structure is considered to be a reactivated early Cretaceous syn-rift fault corresponding to the syn-rift period in the opening of the Black Sea (Okay et al., 2018). Indeed, several large syn-rift half-grabens were mapped in the deepwater of the Central Pontides (Menlikli et al., 2007). Note that the upper segment of the reverse fault has not offset the Eocene strata rather it just produced a kink in it (Fig. 13a).

The discovery well, Akcakoca-1 and two subsequent wells all documented a thick (>1000 m) Paleocene-Eocene sequence above an at least 300 m thick Upper Cretaceous succession (Fig. 13b, Önal and Demirbağ, 2019). This post-rift strata are folded into an asymmetric anticline and truncated by an angular unconformity overlain by Pliocene post-kinematic shales. Whereas the thickness of the syn-rift Lower Cretaceous sequence can be established due to the lack of well-penetrations, we speculate that the thick Upper Cretaceous to Middle Eocene post-rift sequence is probably thicker (circa 2 km). If correct, then the Akcakoca anticline formed as a Mode II inversion structure.

Interestingly, there are structures in the nearby onshore area which we also consider inversion features. The geologic map and the corresponding transect (Aydın et al., 1987) in the onshore Sakarya-Akcakoca area (Fig. 13c and d) were reproduced here to argue that at least two outcropping WNW-ESE structures may represent inversion structures which were severely eroded



down to their core after the middle Eocene uplift of the Central Pontides. We have conceptually added to the transect of Aydın et al. (1987) to show how these structures might have looked like prior to the regional erosion (Fig. 13d).

The onshore examples suggest that the preexisting extensional fabric required for the reverse reactivation during inversion may be older than early Cretaceous. In fact, the section of Aydın et al. (1987) suggests growth for the Triassic sequence for the outboard structure (Fig. 13d). If correct, perhaps the offshore inversion anticlines, striking the same and having the same polarity, may have an older syn-rift core than the inferred Lower Cretaceous strata. If there is a case for a Triassic syn-rift sequence beneath the offshore anticlines that would certainly make them Mode II inversion structures given the very thick (>3000 m) post-rift succession prior to the middle Eocene uplift and erosion.

355 4.2.4 Black Sea, Romania

In the deepwater segment of offshore Romania there is a large biogenic gas find associated with an inversion structure. The discovery on a NE-SW trending 4-way anticline was made by the Domino-1 well in 2012, some 170 km offshore, in 930 m water depth. The Domino play concept (Fig. 12) was described pre-drill by Bega and Ionescu (2009) and post-drill by Tari and Simmons (2018), although the play and the prospect itself were already defined in the early 2000s.

360 The robust closure for the multiple pay zones within the Miocene post-rift sequence is the result of a latest Neogene to Pliocene inversion period above a deep-seated pre-rift basement high (Fig. 12). The apex of the regional Polshkov syn-rift basement high (Robinson et al., 1995; Tari et al., 2009) beneath the Domino anticline is located at 7-8 km depth based on depth migrated regional 2D reflection seismic data (Nikishin et al., 2015) and therefore poorly imaged due to the thick and complex overburden. Therefore, the exact structural relationship between the Polshkov High and the overlying Domino structure is not
 365 easy to interpret confidently. Tari and Simmons (2018) showed a generic play cartoon which highlighted the connection between these structures in the context of positive inversion.

Here we show a more specific structural interpretation of the Domino anticline, even though in a cartoonish fashion, assuming that the Cretaceous syn-rift master fault is located on the inboard flank of the Polshkov High, dipping towards the coastline, to the NW (Fig. 12). Reversal of movement on this large fault plane during the Pliocene may have caused the slightly
 370 asymmetric folding of the entire circa 6-7 km thick post-rift strata. The reverse fault itself must have tipped out within the Paleogene sequence as there is no sign of a major fault propagating up into the folded Neogene sequence (Nikishin et al., 2015).

Therefore, similarly to the New Zealand case study described earlier (Fig. 9), a trishear style deformation within the Neogene sequence may be present on the outboard limb of the Domino structure (Fig. 12). Since the post-rift succession is at least four
 375 times thicker than the underlying syn-rift one, the inversion occurred in Mode II.

As to hydrocarbon exploration, the gas reservoirs of the Domino discovery are Miocene to Pliocene deepwater clastic systems (Bega and Ionescu, 2009; Routh et al., 2017) located within the upper part of the post-rift sequence of the inversion structure. The source for the biogenic gas in the pay intervals is believed to be within post-rift Miocene shales just like in nearby small gas fields located at the shelf edge (e.g. Duley and Fogg, 2009; Olaru et al., 2018). Therefore, the main elements of the



380 petroleum system are entirely located within the post-rift segment of the Mode II inversion structure, just as shown in the generic model of Tari et al. (2020), see Fig. 1b. This example, along with the previous ones, highlights again the importance of this class of inversion structures.

5 Conclusions and outlook

385 Based on our physical experiments performed to address the influence of the syn- versus post-rift thickness ratio (Mode I and II) and the degree of positive inversion, we observe that this ratio does not seem to have a major influence on the inversion-related structures if the reverse movement on the preexisting listric fault is relatively large. Still, the performed experiments have no more than 2:1 post-rift to syn-rift ratios, thus there is a need for further investigation.

The structural patterns show that the style and propagation of contractional structures into the post-rift cover sequence is primarily affected by the amount of reverse movement along the inherited listric fault. Based on observations on natural 390 examples from different parts of the world, a much thicker post-rift cover compared to that of the underlying syn-rift (at least 3-4) tend to inhibit the propagation of thrust faults up-section, causing the reverse fault to tip out with a trishear deformation zone ahead of it. These Mode II inversion structures manifest themselves as slightly asymmetric large folds at higher post-rift stratigraphic levels.

395 Additional modelling with post-rift to syn-rift ratios higher than 2:1 are required to fully reproduce the geometries seen in New Zealand, Israel, Turkey and Romania, where the reverse fault tipped out in the lower part of the post-rift sequence and the Mode II inversion produced very large and only slightly asymmetric folds several kilometres above the underlying much thinner syn-rift nucleus.

The documentation of the expected trishear deformation style in the frontal limb of the inversion anticlines in a new set of physical experiments provides an additional challenge. These observations presented in this paper have a direct impact on the 400 understanding of the geo-energy systems associated with inverted structures.

Author contribution: GT conceptualized the project. AT and DMT designed and carried them out the experiments. GT provided and interpreted natural examples. CK, AL and ZS contributed to discussions and revisions of manuscript. AT, DMT and GT wrote the original draft and prepared the manuscript with contributions from all co-authors.

405 Acknowledgements

We thank Frank Zwaan for inviting us to contribute this paper to the special issue of Solid Earth and for their editorial efforts. Discussions concerning inversion tectonics with the late Albert Bally, Bill Bosworth, Troy Collier, Dana-Stefania Constandache, Kia Fallah, Callum Kennedy, Jan Mayer, Aral Okay, Andrew Robinson and Alexander Wunderlich are greatly appreciated.



410 Competing interests

The contact author has declared that none of the authors has any competing interests.

References

- Adam, J., Urai, J. L., Wieneke, B., Oncken, O., Pfeiffer, K., Kukowski, N., Lohrmann, J., Hoth, S., van der Zee, W., and Schmatz, J.: Shear localisation and strain distribution during tectonic faulting—new insights from granular-flow experiments and high-resolution optical image correlation techniques, *J. Struct. Geol.*, 27, 283–301, <https://doi.org/10.1016/j.jsg.2004.08.008>, 2005.
- Alaygut, D., Teymur, S., Seker, H., Akoz, O., Oner, A., and Sarginalp, M.: Depositional model and reservoir features of the Eocene sandstones in the Akcakoca area: West Black Sea region, Turkey, in: AAPG Search and Discovery Article #90024, AAPG Regional International Conference, Istanbul, Turkey, 2004.
- 420 Allmendinger, R. W.: Inverse and forward numerical modeling of trishear fault-propagation folds, *Tectonics*, 17, 640–656, <https://doi.org/10.1029/98TC01907>, 1998.
- Aydın, M., Serdar, H. S., Şahintürk, Ö., Yazman, M., Çokuğraş, R., Demir, O., and Özçelik, Y.: The geology of the Çamdağ (Sakarya)-Sünnicedağ (Bolu) region, *Bull. Geol. Soc. Turk.*, 30, 1–14, 1987.
- 425 Badley, M. E., Price, J. D., and Backshall, L. C.: Inversion, reactivated faults and related structures: seismic examples from the southern North Sea, *Geol. Soc. Lond. Spec. Publ.*, 44, 201–219, <https://doi.org/10.1144/GSL.SP.1989.044.01.12>, 1989.
- Bally, A. W.: Tectogénèse et sismique réflexion, *Bull. Société Géologique Fr.*, 29, 279–285, 1984.
- Bega, Z. and Ionescu, G.: Neogene structural styles of the NW Black Sea region, offshore Romania, *Lead. Edge*, 28, 1082–1089, <https://doi.org/10.1190/1.3236378>, 2009.
- Bevan, T. G. and Moustafa, A. R.: Inverted rift-basins of northern Egypt, in: *Regional Geology and Tectonics: Phanerozoic Rift Systems and Sedimentary Basins*, Elsevier, 482–507, <https://doi.org/10.1016/B978-0-444-56356-9.00018-3>, 2012.
- 430 Bonini, M., Sani, F., and Antonielli, B.: Basin inversion and contractional reactivation of inherited normal faults: A review based on previous and new experimental models, *Tectonophysics*, 522–523, 55–88, <https://doi.org/10.1016/j.tecto.2011.11.014>, 2012.
- Bosworth, W. and Tari, G.: Hydrocarbon accumulation in basins with multiple phases of extension and inversion: examples from the Western Desert (Egypt) and the western Black Sea, *Solid Earth*, 12, 59–77, <https://doi.org/10.5194/se-12-59-2021>, 2021.
- 435 Bosworth, W., Guiraud, R., and Kessler, L. G.: Late Cretaceous (ca. 84 Ma) compressive deformation of the stable platform of northeast Africa (Egypt): Far-field stress effects of the “Santonian event” and origin of the Syrian arc deformation belt, *Geology*, 27, 633, [https://doi.org/10.1130/0091-7613\(1999\)027<0633:LCCMCD>2.3.CO;2](https://doi.org/10.1130/0091-7613(1999)027<0633:LCCMCD>2.3.CO;2), 1999.
- 440 Buchanan, P. G. and McClay, K. R.: Sandbox experiments of inverted listric and planar fault systems, *Tectonophysics*, 188, 97–115, [https://doi.org/10.1016/0040-1951\(91\)90317-L](https://doi.org/10.1016/0040-1951(91)90317-L), 1991.



- Butter, S. J. H., Pfiffner, O. A., and Beaumont, C.: Inversion of extensional sedimentary basins: A numerical evaluation of the localisation of shortening, *Earth Planet. Sci. Lett.*, 288, 492–504, <https://doi.org/10.1016/j.epsl.2009.10.011>, 2009.
- 445 Cooper, M. and Warren, M. J.: The geometric characteristics, genesis and petroleum significance of inversion structures, *Geol. Soc. Lond. Spec. Publ.*, 335, 827–846, <https://doi.org/10.1144/SP335.33>, 2010.
- Cooper, M. and Warren, M. J.: Inverted fault systems and inversion tectonic settings, in: *Regional Geology and Tectonics: Principles of Geologic Analysis*, Elsevier, 169–204, <https://doi.org/10.1016/B978-0-444-64134-2.00009-2>, 2020.
- Cubas, N., Barnes, C., and Maillot, B.: Inverse method applied to a sand wedge: Estimation of friction parameters and uncertainty analysis, *J. Struct. Geol.*, 55, 101–113, <https://doi.org/10.1016/j.jsg.2013.07.003>, 2013.
- 450 Dichiarante, A. M., Holdsworth, R. E., Dempsey, E. D., McCaffrey, K. J. W., and Utley, T. A. G.: Outcrop-scale manifestations of reactivation during multiple superimposed rifting and basin inversion events: the Devonian Orcadian Basin, northern Scotland, *J. Geol. Soc.*, 178, jgs2020-089, <https://doi.org/10.1144/jgs2020-089>, 2021.
- Dinu, C., Wong, H. K., Tambrea, D., and Matenco, L.: Stratigraphic and structural characteristics of the Romanian Black Sea shelf, *Tectonophysics*, 410, 417–435, <https://doi.org/10.1016/j.tecto.2005.04.012>, 2005.
- 455 Dooley, T. P. and Hudec, M. R.: Extension and inversion of salt-bearing rift systems, *Solid Earth*, 11, 1187–1204, <https://doi.org/10.5194/se-11-1187-2020>, 2020.
- Duley, P. and Fogg, A.: Old dogs and new tricks; unlocking the hydrocarbon potential of the Romanian Black Sea: Ana and Doina gas fields and the role of inversion in derisking, *Lead. Edge*, 28, 1091–1096, 2009.
- Ellis, P. G. and McClay, K. R.: Listric extensional fault systems - results of analogue model experiments, *Basin Res.*, 1, 55–70, <https://doi.org/10.1111/j.1365-2117.1988.tb00005.x>, 1988.
- 460 Erslev, E. A.: Trishear fault-propagation folding, *Geology*, 19, 617, [https://doi.org/10.1130/0091-7613\(1991\)019<0617:TFPF>2.3.CO;2](https://doi.org/10.1130/0091-7613(1991)019<0617:TFPF>2.3.CO;2), 1991.
- Ferrer, O., McClay, K., and Sellier, N. C.: Influence of fault geometries and mechanical anisotropies on the growth and inversion of hangingwall synclinal basins: insights from sandbox models and natural examples, *Geol. Soc. Lond. Spec. Publ.*, 439, 487–509, <https://doi.org/10.1144/SP439.8>, 2017.
- 465 Gardosh, M. A. and Tannenbaum, E.: The Petroleum Systems of Israel, in: *Memoir 106: Petroleum Systems of the Tethyan Region*, edited by: Marlow, L., Kendall, C. C. G., and Rose, L. A., AAPG, <https://doi.org/10.1306/13431857M106298>, 2014.
- Gardosh, M. A., Garfunkel, Z., Druckman, Y., and Buchbinder, B.: Tethyan rifting in the Levant Region and its role in Early Mesozoic crustal evolution, *Geol. Soc. Lond. Spec. Publ.*, 341, 9–36, <https://doi.org/10.1144/SP341.2>, 2010.
- 470 Giba, M., Nicol, A., and Walsh, J. J.: Evolution of faulting and volcanism in a back-arc basin and its implications for subduction processes: TARANAKI BASIN EVOLUTION, *Tectonics*, 29, n/a-n/a, <https://doi.org/10.1029/2009TC002634>, 2010.
- Gillcrist, R., Coward, M., and Mugnier, J.-L.: Structural inversion and its controls : examples from the Alpine foreland and the French Alps, *Geodin. Acta*, 1, 5–34, <https://doi.org/10.1080/09853111.1987.11105122>, 1987.
- 475 Gomes, C. J. S., Danderfer Filho, A., Posada, A. M. A., and Silva, A. C. da: The role of backstop shape during inversion tectonics physical models, *An. Acad. Bras. Ciênc.*, 82, 997–1012, <https://doi.org/10.1590/S0001-37652010000400021>, 2010.



- Granado, P. and Ruh, J. B.: Numerical modelling of inversion tectonics in fold-and-thrust belts, *Tectonophysics*, 763, 14–29, <https://doi.org/10.1016/j.tecto.2019.04.033>, 2019.
- Harding, T. P.: Seismic Characteristics and Identification of Negative Flower Structures, Positive Flower Structures, and Positive Structural Inversion, *AAPG Bull.*, 69, <https://doi.org/10.1306/AD462538-16F7-11D7-8645000102C1865D>, 1985.
- 480 Hardy, S. and Ford, M.: Numerical modeling of trishear fault propagation folding, *Tectonics*, 16, 841–854, <https://doi.org/10.1029/97TC01171>, 1997.
- Khriachtchevskaia, O., Stovba, S., and Popadyuk, I.: Hydrocarbon prospects in the Western Black Sea of Ukraine, *Lead. Edge*, 28, 1024–1029, <https://doi.org/10.1190/1.3236371>, 2009.
- 485 Khriachtchevskaia, O., Stovba, S., and Stephenson, R.: Cretaceous–Neogene tectonic evolution of the northern margin of the Black Sea from seismic reflection data and tectonic subsidence analysis, *Geol. Soc. Lond. Spec. Publ.*, 340, 137–157, <https://doi.org/10.1144/SP340.8>, 2010.
- Koopman, A., Speksnijder, A., and Horsfield, W. T.: Sandbox model studies of inversion tectonics, *Tectonophysics*, 137, 379–388, [https://doi.org/10.1016/0040-1951\(87\)90329-5](https://doi.org/10.1016/0040-1951(87)90329-5), 1987.
- 490 Korucu, Ö., Sipahioğlu, N. Ö., Aktepe, S., and Bengü, E.: Correlation and determination of Neogene sequences employing recent ultra-deep wells in Western-Central part of Turkish Black Sea, *AAPG Europe Regional Conference*, Tbilisi, 12–19, 2013.
- Krezsek, C., Bercea, R.-I., Tari, G., and Ionescu, G.: Cretaceous sedimentation along the Romanian margin of the Black Sea: inferences from onshore to offshore correlations, *Geol. Soc. Lond. Spec. Publ.*, 464, 211–245, <https://doi.org/10.1144/SP464.10>, 2018.
- 495 Krzywiec, P., Gutowski, J., Walaszczyk, I., Wróbel, G., and Wybraniec, S.: Tectonostratigraphic model of the late cretaceous inversion along the Nowe Miasto-Zawichost fault zone, *SE Mid-Polish trough*, *Geol. Q.*, 53, 27–48, 2009.
- Krzywiec, P., Stachowska, A., and Stypa, A.: The only way is up – on Mesozoic uplifts and basin inversion events in SE Poland, *Geol. Soc. Lond. Spec. Publ.*, 469, 33–57, <https://doi.org/10.1144/SP469.14>, 2018.
- Lamplugh, G. W.: Structure of the Weald and analogous tracts, *Q. J. Geol. Soc. Lond.*, 75, 1919.
- 500 Macgregor, D. S.: Hydrocarbon habitat and classification of inverted rift basins, *Geol. Soc. Lond. Spec. Publ.*, 88, 83–93, <https://doi.org/10.1144/GSL.SP.1995.088.01.06>, 1995.
- Mattioni, L., Sassi, W., and Callot, J.-P.: Analogue models of basin inversion by transpression: role of structural heterogeneity, *Geol. Soc. Lond. Spec. Publ.*, 272, 397–417, <https://doi.org/10.1144/GSL.SP.2007.272.01.20>, 2007.
- 505 McClay, K. R.: Analogue models of inversion tectonics, *Geol. Soc. Lond. Spec. Publ.*, 44, 41–59, <https://doi.org/10.1144/GSL.SP.1989.044.01.04>, 1989.
- McClay, K. R.: The geometries and kinematics of inverted fault systems: a review of analogue model studies, *Geol. Soc. Lond. Spec. Publ.*, 88, 97–118, <https://doi.org/10.1144/GSL.SP.1995.088.01.07>, 1995.
- McClay, K. R. and Buchanan, P. G.: Thrust faults in inverted extensional basins, in: *Thrust Tectonics*, edited by: McClay, K. R., Springer Netherlands, Dordrecht, 93–104, https://doi.org/10.1007/978-94-011-3066-0_8, 1992.



- 510 Menlikli, C., Demirer, A., Sipahioğlu, Ö., Körpe, L., and Aydemir, V.: Exploration plays in the Turkish Black Sea, *Lead. Edge*, 28, 1066–1075, <https://doi.org/10.1190/1.3236376>, 2009.
- Mitra, S. and Islam, Q. T.: Experimental (clay) models of inversion structures, *Tectonophysics*, 230, 211–222, [https://doi.org/10.1016/0040-1951\(94\)90136-8](https://doi.org/10.1016/0040-1951(94)90136-8), 1994.
- 515 Molnar, N. and Buiter, S.: Analogue modelling of the inversion of multiple extensional basins in foreland fold-and-thrust belts, Tectonic plate interactions, magma genesis, and lithosphere deformation at all scales/Structural geology and tectonics, paleoseismology, rock physics, experimental deformation/Structural geology, <https://doi.org/10.5194/egusphere-2022-1014>, 2022.
- Munteanu, I., Matenco, L., Dinu, C., and Cloetingh, S.: Kinematics of back-arc inversion of the Western Black Sea Basin: BACK-ARC INVERSION, BLACK SEA, *Tectonics*, 30, n/a-n/a, <https://doi.org/10.1029/2011TC002865>, 2011.
- 520 Needham, D. L., Pettingill, H. S., Christensen, C. J., French, J., and Karcz, Z. (Kul): The Tamar Giant Gas Field: Opening the Subsalt Miocene Gas Play in the Levant Basin, in: Giant Fields of the Decade 2000–2010, The American Association of Petroleum Geologists, <https://doi.org/10.1306/13572009M1133688>, 2017.
- Nicol, A., Mazengarb, C., Chanier, F., Rait, G., Uruski, C., and Wallace, L.: Tectonic evolution of the active Hikurangi subduction margin, New Zealand, since the Oligocene: HIKURANGI SUBDUCTION MARGIN TECTONICS, *Tectonics*, 26, n/a-n/a, <https://doi.org/10.1029/2006TC002090>, 2007.
- 525 Nikishin, A. M., Okay, A. I., Tüysüz, O., Demirer, A., Amelin, N., and Petrov, E.: The Black Sea basins structure and history: New model based on new deep penetration regional seismic data. Part 1: Basins structure and fill, *Mar. Pet. Geol.*, 59, 638–655, <https://doi.org/10.1016/j.marpetgeo.2014.08.017>, 2015.
- Okay, A. I., Altiner, D., Sunal, G., Aygöl, M., Akdoğan, R., Altiner, S., and Simmons, M.: Geological evolution of the Central Pontides, *Geol. Soc. Lond. Spec. Publ.*, 464, 33–67, <https://doi.org/10.1144/SP464.3>, 2018.
- 530 Olaru, R., Krézsek, C., Rainer, T. M., Ungureanu, C., Turi, V., Ionescu, G., and Tari, G.: 3D BASIN MODELLING OF OLIGOCENE – MIOCENE MAIKOP SOURCE ROCKS OFFSHORE ROMANIA AND IN THE WESTERN BLACK SEA, *J. Pet. Geol.*, 41, 351–365, <https://doi.org/10.1111/jpg.12707>, 2018.
- Önal, K. M. and Demirbag, E.: New evidences of compressional tectonic regime at the southern part of the Western Black Sea Basin offshore Akçakoca-Cide, *Istanb. J. Geosci.*, 30, 27–51, 2019.
- 535 Panien, M., Schreurs, G., and Pfiffner, A.: Sandbox experiments on basin inversion: testing the influence of basin orientation and basin fill, *J. Struct. Geol.*, 27, 433–445, <https://doi.org/10.1016/j.jsg.2004.11.001>, 2005.
- Phillips, T. B., Jackson, C. A.-L., and Norcliffe, J. R.: Pre-inversion normal fault geometry controls inversion style and magnitude, Farsund Basin, offshore southern Norway, *Solid Earth*, 11, 1489–1510, <https://doi.org/10.5194/se-11-1489-2020>, 2020.
- 540 Reilly, C., Nicol, A., and Walsh, J.: Importance of preexisting fault size for the evolution of an inverted fault system, *Geol. Soc. Lond. Spec. Publ.*, 439, 447–463, <https://doi.org/10.1144/SP439.2>, 2017.
- Roberts, D. G.: Basin inversion in and around the British Isles, *Geol. Soc. Lond. Spec. Publ.*, 44, 131–150, <https://doi.org/10.1144/GSL.SP.1989.044.01.09>, 1989.



- 545 Roberts, G. and Peace, D.: Hydrocarbon plays and prospectivity of the Levantine Basin, offshore Lebanon and Syria from modern seismic data, *GeoArabia*, 12, 99–124, <https://doi.org/10.2113/geoarabia120399>, 2007.
- Robinson, A., Spadini, G., Cloetingh, S., and Rudat, J.: Stratigraphic evolution of the Black Sea: inferences from basin modelling, *Mar. Pet. Geol.*, 12, 821–835, [https://doi.org/10.1016/0264-8172\(95\)98850-5](https://doi.org/10.1016/0264-8172(95)98850-5), 1995.
- Robinson, A. G. and Kerusov, E.: Stratigraphic and Structural Development of the Gulf of Odessa, Ukrainian Black Sea: Implications for Petroleum Exploration, in: *Regional and Petroleum Geology of the Black Sea and Surrounding Region*, American Association of Petroleum Geologists, 369–380, <https://doi.org/10.1306/M68612C19>, 1997.
- 550 Roma, M., Ferrer, O., McClay, K. R., Munoz, J. A., Roca, E., Gratacos, O., and Cabello, P.: Weld kinematics of syn-rift salt during basement-involved extension and subsequent inversion: Results from analog models, *Geol. Acta*, 16, 391–410, <https://doi.org/10.1344/GeologicaActa2018.16.4.4>, 2018.
- 555 Routh, P., Neelamani, R., Lu, R., Lazaratos, S., Braaksma, H., Hughes, S., Saltzer, R., Stewart, J., Naidu, K., Averill, H., Gottumukkula, V., Homonko, P., Reilly, J., and Leslie, D.: Impact of high-resolution FWI in the Western Black Sea: Revealing overburden and reservoir complexity, *Lead. Edge*, 36, 60–66, <https://doi.org/10.1190/tle36010060.1>, 2017.
- Sieberer, A.-K., Willingshofer, E., Klotz, T., Ortner, H., and Pomella, H.: Inversion of extensional basins parallel and oblique to their boundaries: Inferences from analogue models and field observations from the Dolomites Indenter, eastern Southern Alps, Tectonic plate interactions, magma genesis, and lithosphere deformation at all scales/Structural geology and tectonics, paleoseismology, rock physics, experimental deformation/Tectonics, <https://doi.org/10.5194/egusphere-2022-1530>, 2023.
- 560 Stovba, S. M., Popadyuk, I. V., Fenota, P. O., and Khriachtchevskaia, O. I.: Geological structure and tectonic evolution of the Ukrainian sector of the Black Sea, *Geofiz. Zhurnal*, 42, 53–106, <https://doi.org/10.24028/gzh.0203-3100.v42i5.2020.215072>, 2020.
- 565 Tamas, A., Holdsworth, R. E., Underhill, J. R., Tamas, D. M., Dempsey, E. D., Hardman, K., Bird, A., McCarthy, D., McCaffrey, K. J. W., and Selby, D.: New onshore insights into the role of structural inheritance during Mesozoic opening of the Inner Moray Firth Basin, Scotland, *J. Geol. Soc.*, 179, jgs2021-066, <https://doi.org/10.1144/jgs2021-066>, 2022a.
- Tamas, A., Holdsworth, R. E., Underhill, J. R., Tamas, D. M., Dempsey, E. D., McCarthy, D. J., McCaffrey, K. J. W., and Selby, D.: Correlating deformation events onshore and offshore in superimposed rift basins: The Lossiemouth Fault Zone, Inner Moray Firth Basin, Scotland, *Basin Res.*, 34, 1314–1340, <https://doi.org/10.1111/bre.12661>, 2022b.
- 570 Tămaş, D. M., Schléder, Z., Tămaş, A., Krézsek, C., Copoţ, B., and Filipescu, S.: Middle Miocene evolution and structural style of the Diapir Fold Zone, Eastern Carpathian Bend Zone, Romania: insights from scaled analogue modelling, *Geol. Soc. Lond. Spec. Publ.*, SP490-2019–091, <https://doi.org/10.1144/SP490-2019-091>, 2020.
- Tari, G., Davies, J., Dellmour, R., Larratt, E., Novotny, B., and Kozhuharov, E.: Play types and hydrocarbon potential of the deepwater Black Sea, NE Bulgaria, *Lead. Edge*, 28, 1076–1081, <https://doi.org/10.1190/1.3236377>, 2009.
- 575 Tari, G., Arbouille, D., Schléder, Z., and Tóth, T.: Inversion tectonics: a brief petroleum industry perspective, *Solid Earth*, 11, 1865–1889, <https://doi.org/10.5194/se-11-1865-2020>, 2020.
- Tari, G. C. and Simmons, M. D.: History of deepwater exploration in the Black Sea and an overview of deepwater petroleum play types, *Geol. Soc. Lond. Spec. Publ.*, 464, 439–475, <https://doi.org/10.1144/SP464.16>, 2018.
- 580 Turner, J. P. and Williams, G. A.: Sedimentary basin inversion and intra-plate shortening, *Earth-Sci. Rev.*, 65, 277–304, <https://doi.org/10.1016/j.earscirev.2003.10.002>, 2004.



- Tüysüz, O.: Cretaceous geological evolution of the Pontides, *Geol. Soc. Lond. Spec. Publ.*, 464, 69–94, <https://doi.org/10.1144/SP464.9>, 2018.
- 585 Uzkeda, H., Poblet, J., Bulnes, M., and Martín, S.: Effects of inherited structures on inversion tectonics: Examples from the Asturian Basin (NW Iberian Peninsula) interpreted in a Computer Assisted Virtual Environment (CAVE), *Geosphere*, 14, 1635–1656, <https://doi.org/10.1130/GES01609.1>, 2018.
- Walley, C. D.: Some outstanding issues in the geology of Lebanon and their importance in the tectonic evolution of the Levantine region, *Tectonophysics*, 298, 37–62, [https://doi.org/10.1016/S0040-1951\(98\)00177-2](https://doi.org/10.1016/S0040-1951(98)00177-2), 1998.
- 590 Wunderlich, A. and Mayer, J.: Sequential fault movement and sequence stratigraphic implications on linked depositional systems in a multi-phase rift, Central and Southern Taranaki Basin, New Zealand, in: EAGE/AAPG Workshop on Reducing Exploration Risk in Rift Basins, EAGE/AAPG Workshop on Reducing Exploration Risk in Rift Basins, Kuala Lumpur, Malaysia, 1–2, <https://doi.org/10.3997/2214-4609.202076007>, 2019.
- 595 Wunderlich, A., Fohrmann, M., Mayer, J., Clare, A., and Howlett, A.: Depositional Architecture, Sequence Stratigraphy and the Quantification of Hydrodynamic Fractionation as a Tool for the Prediction of Reservoir Quality in a Deep Marine System: An Example from the Miocene Moki Formation in the Maari/Manaia Field Area, Southern Taranaki Basin, New Zealand, in: Proceedings of the 2019 South East Asia Petroleum Exploration Society (SEAPEX) Conference, Southeast Asia Petroleum Exploration Society (SEAPEX), 35a, 2019.
- Yamada, Y. and McClay, K. R.: 3-D Analog Modeling of Inversion Thrust Structures, in: *Thrust Tectonics and Hydrocarbon Systems*, American Association of Petroleum Geologists, 281–306, <https://doi.org/10.1306/M82813C16>, 2004.
- 600 Zwaan, F., Schreurs, G., Buitert, S. J. H., Ferrer, O., Reitano, R., Rudolf, M., and Willingshofer, E.: Analogue modelling of basin inversion: a review and future perspectives, *Solid Earth*, 13, 1859–1905, <https://doi.org/10.5194/se-13-1859-2022>, 2022.

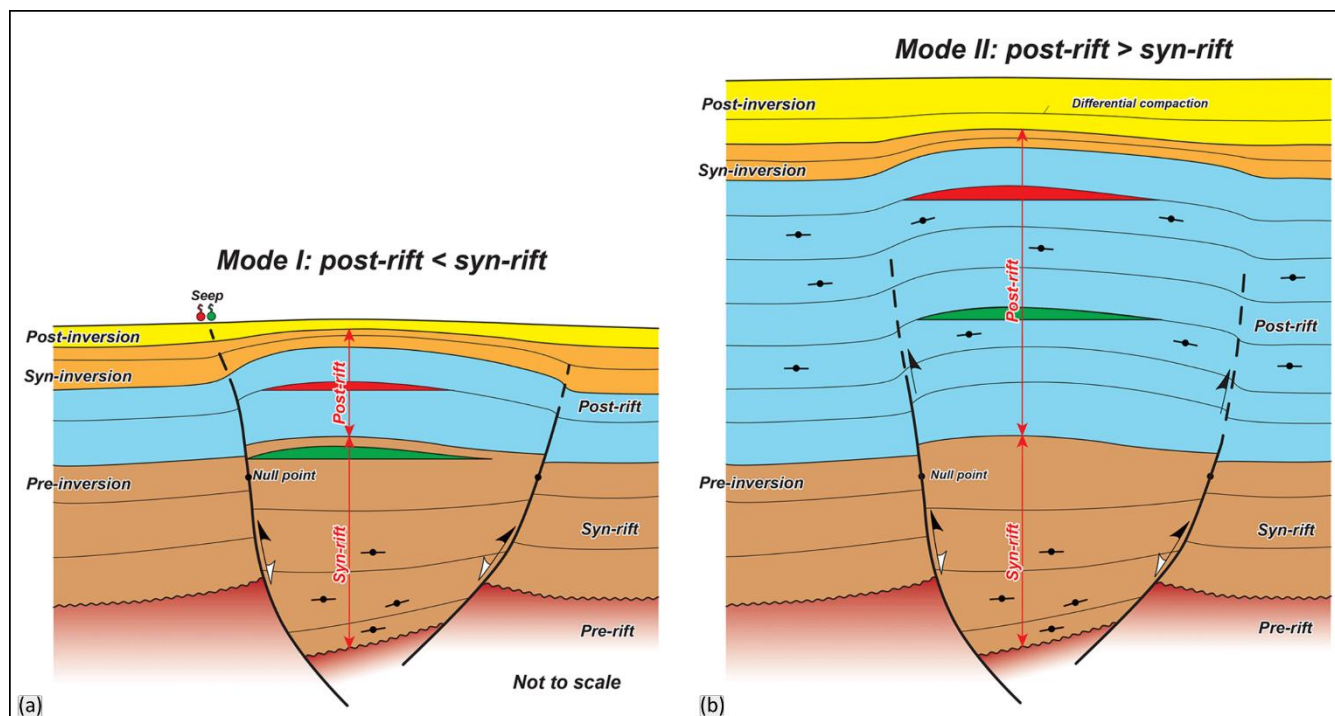


Figure 1. Conceptual models showing Mode I and Mode II inversion (after Tari et al., 2020).

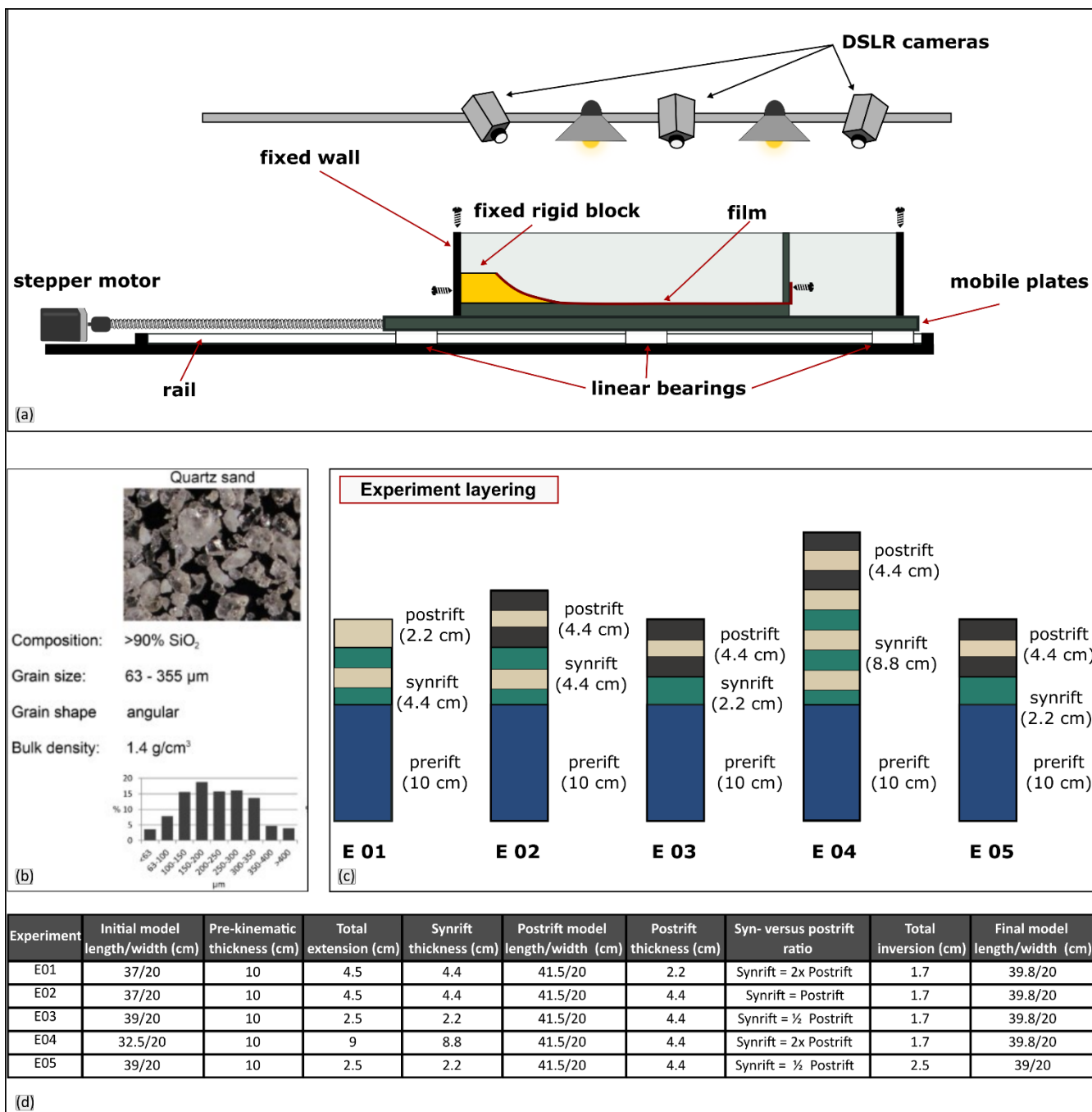
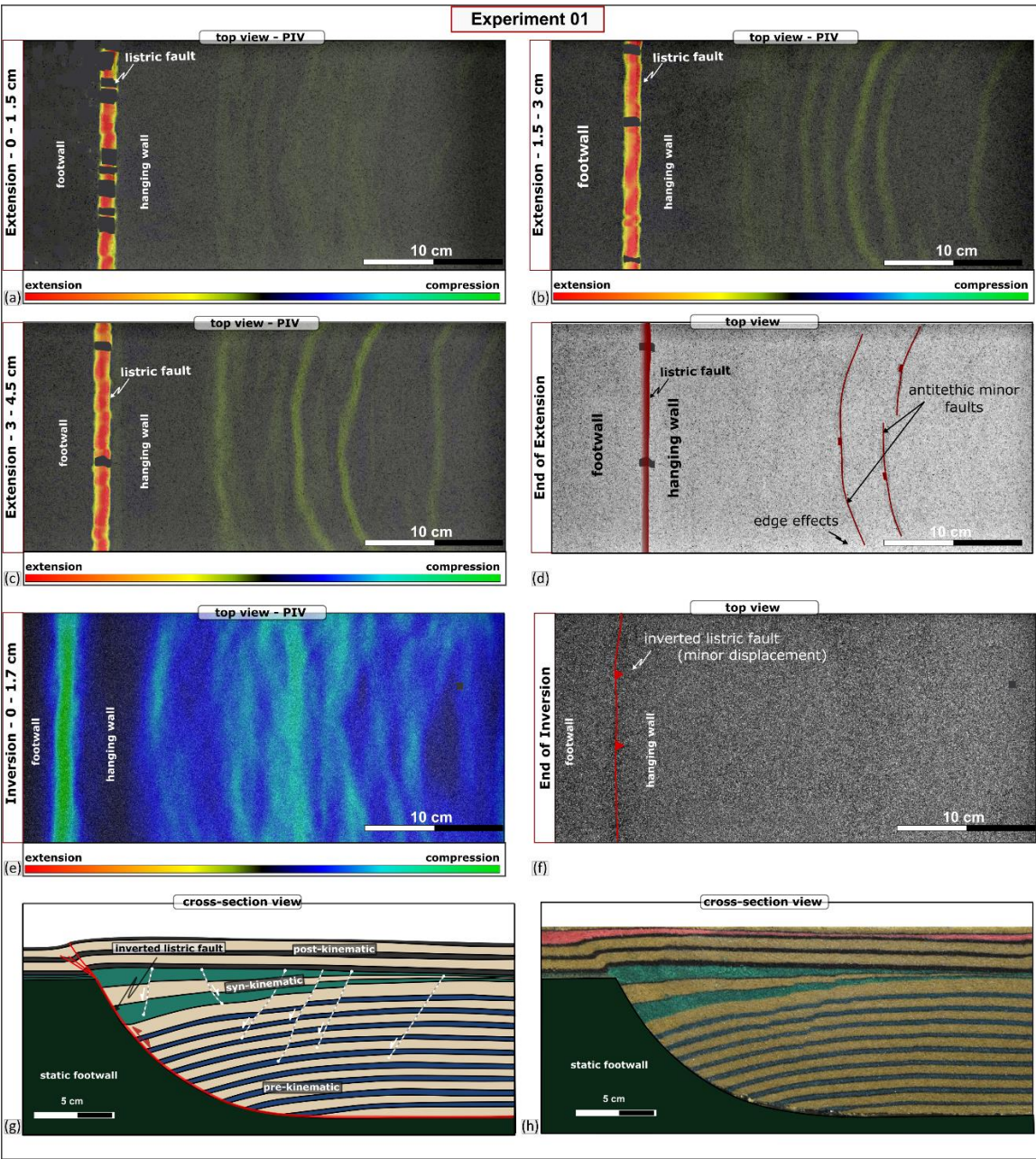


Figure 2. Side view of experimental box and monitoring. b) Properties of the granular material used for the experiments (Tămaş et al., 2020). c) Experiment layering. d) Summary of the experiment setup.



610

615

Figure 3. Results of Experiment 1 showing (a-c) the PIV map during syn-sedimentary phase displaying high extensional strain associated with the listric fault (bright red) and areas with (a) diffuse extensional strain (yellow) and (b, c) localised extensional strain in the crestal collapse block. d) Top view of Experiment 1 at the end of extension. e) PIV map during inversion phase displaying high compressional strain above the inverted listric fault (bright green) and areas with diffuse to localised compressional strain (green). f) Top view of Experiment 1 at the end of inversion. (g) Interpreted and (h) uninterpreted cross-section through the experiment.

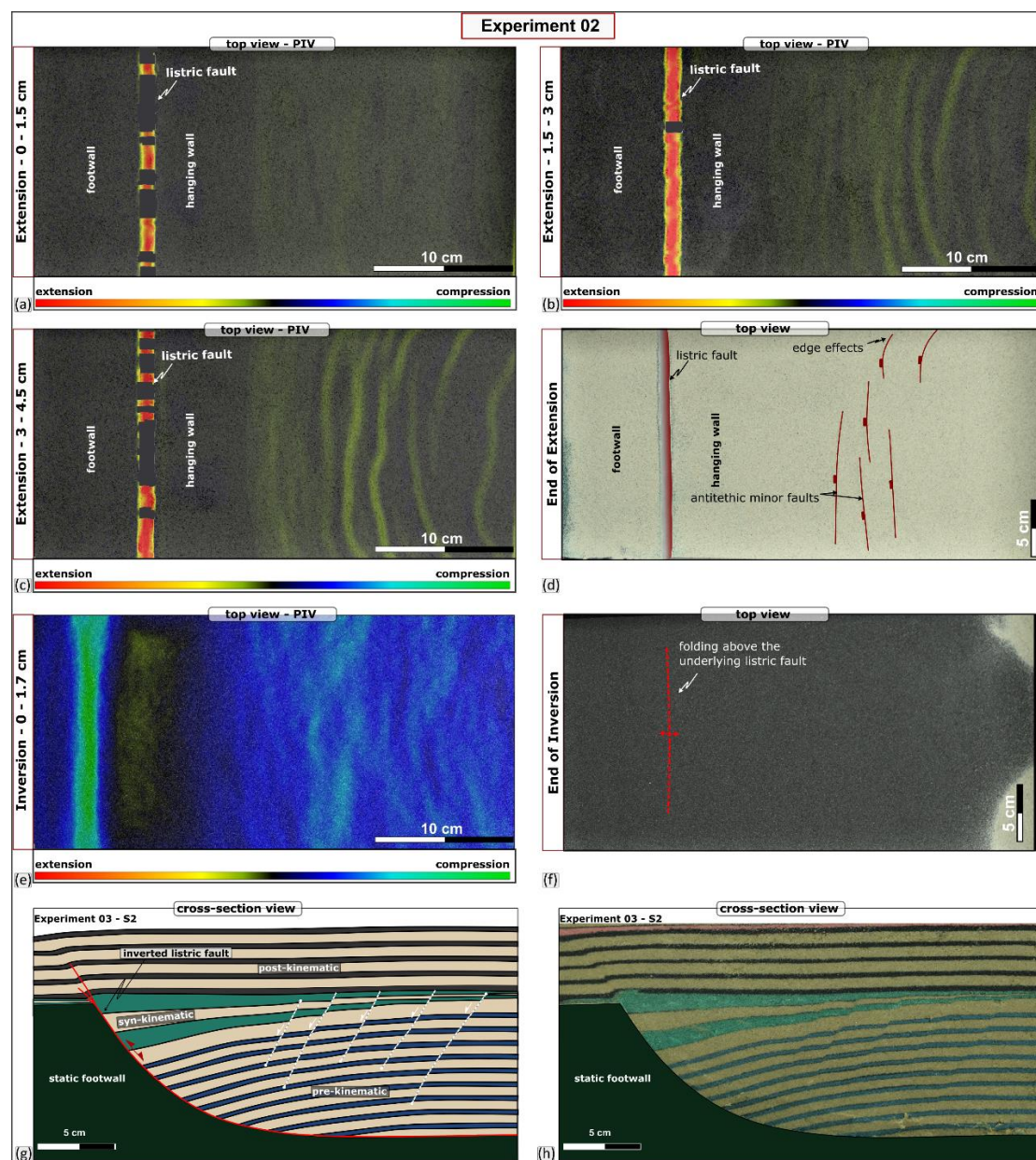


Figure 4. Results of Experiment 2 showing (a-c) the PIV map during syn-sedimentary phase displaying high extensional strain associated with the listric fault (bright red) and areas with (a) diffuse extensional strain (yellow) and (b, c) localised extensional strain in the crestal collapse block. d) Top view of Experiment 2 at the end of extension. e) PIV map during inversion phase displaying high compressional strain above the inverted listric fault (bright green) and areas with diffuse compressional strain (teal). f) Top view of Experiment 2 at the end of inversion (g) Interpreted and (h) uninterpreted cross-section through the experiment.

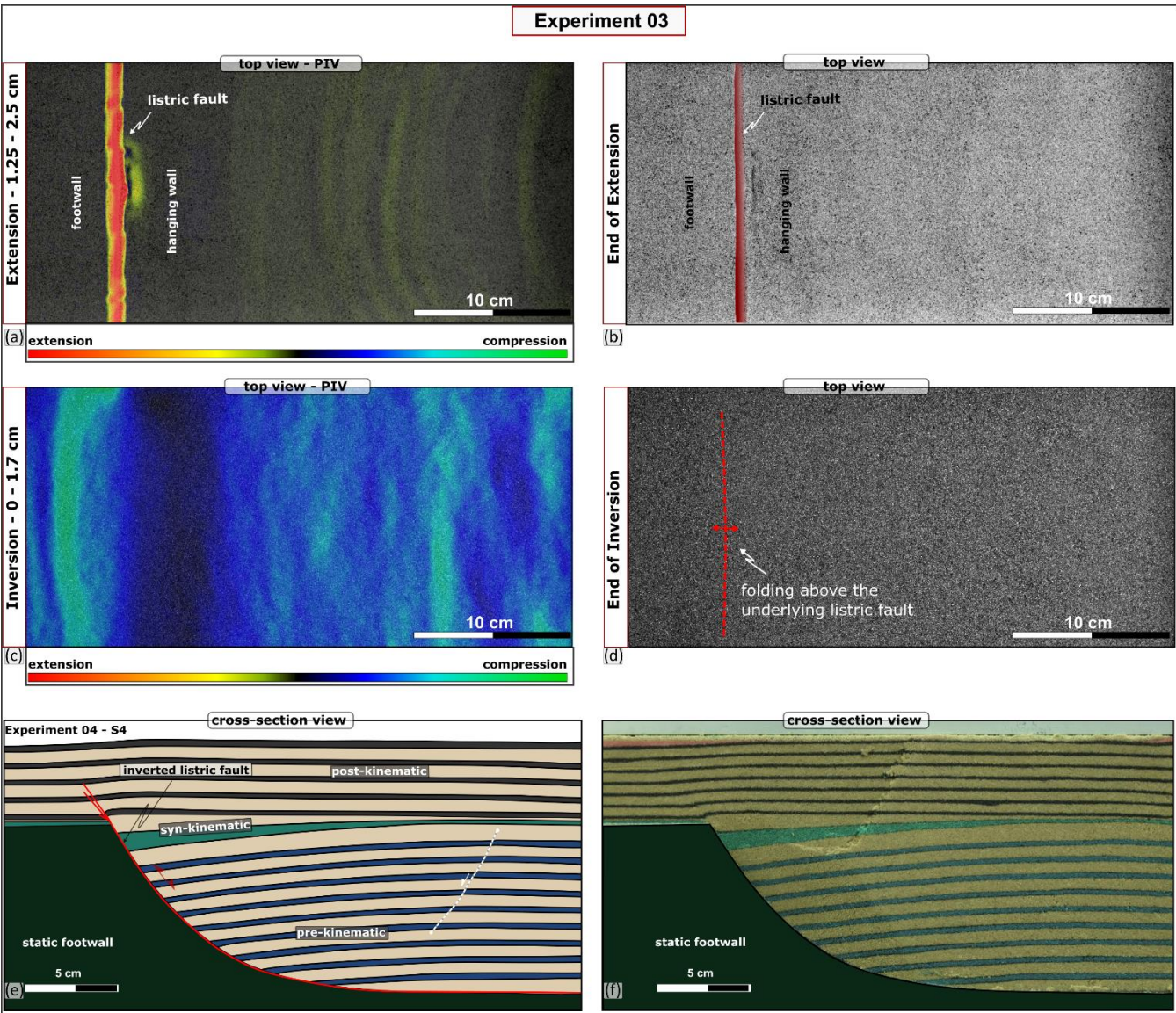


Figure 5. Results of Experiment 3 showing (a) the PIV map during syn-sedimentary phase displaying high extensional strain associated with the listric fault (bright red) and areas with diffuse to more localised extensional strain (yellow) in the crestal collapse block. b) Top view of Experiment 3 at the end of extension. c) PIV map during inversion phase displaying high compressional strain above the inverted listric fault (bright green) and areas with diffuse to more localised compressional strain (teal). d) Top view of Experiment 3 at the end of inversion. (e) Interpreted and (f) uninterpreted cross-section through the experiment.

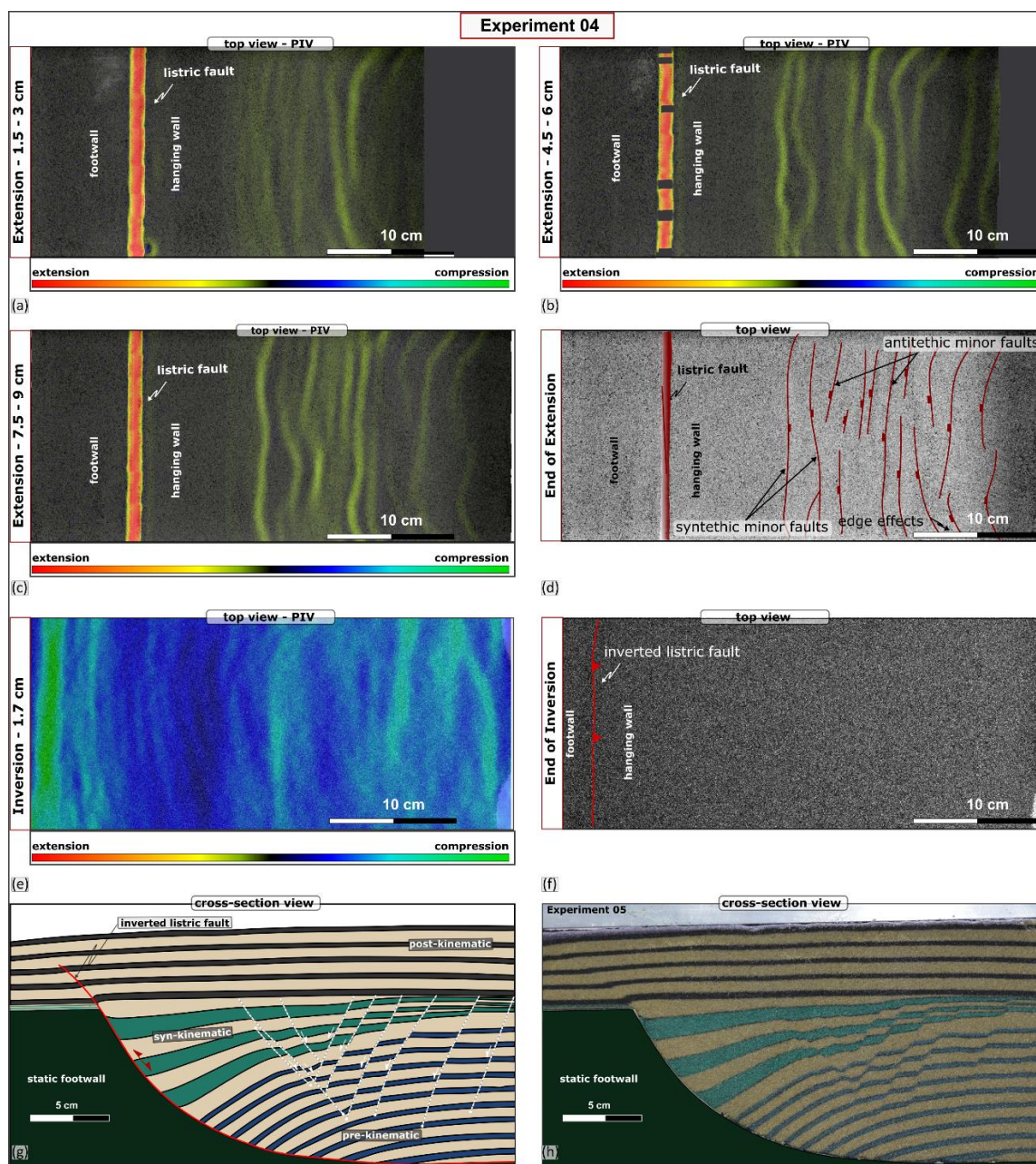
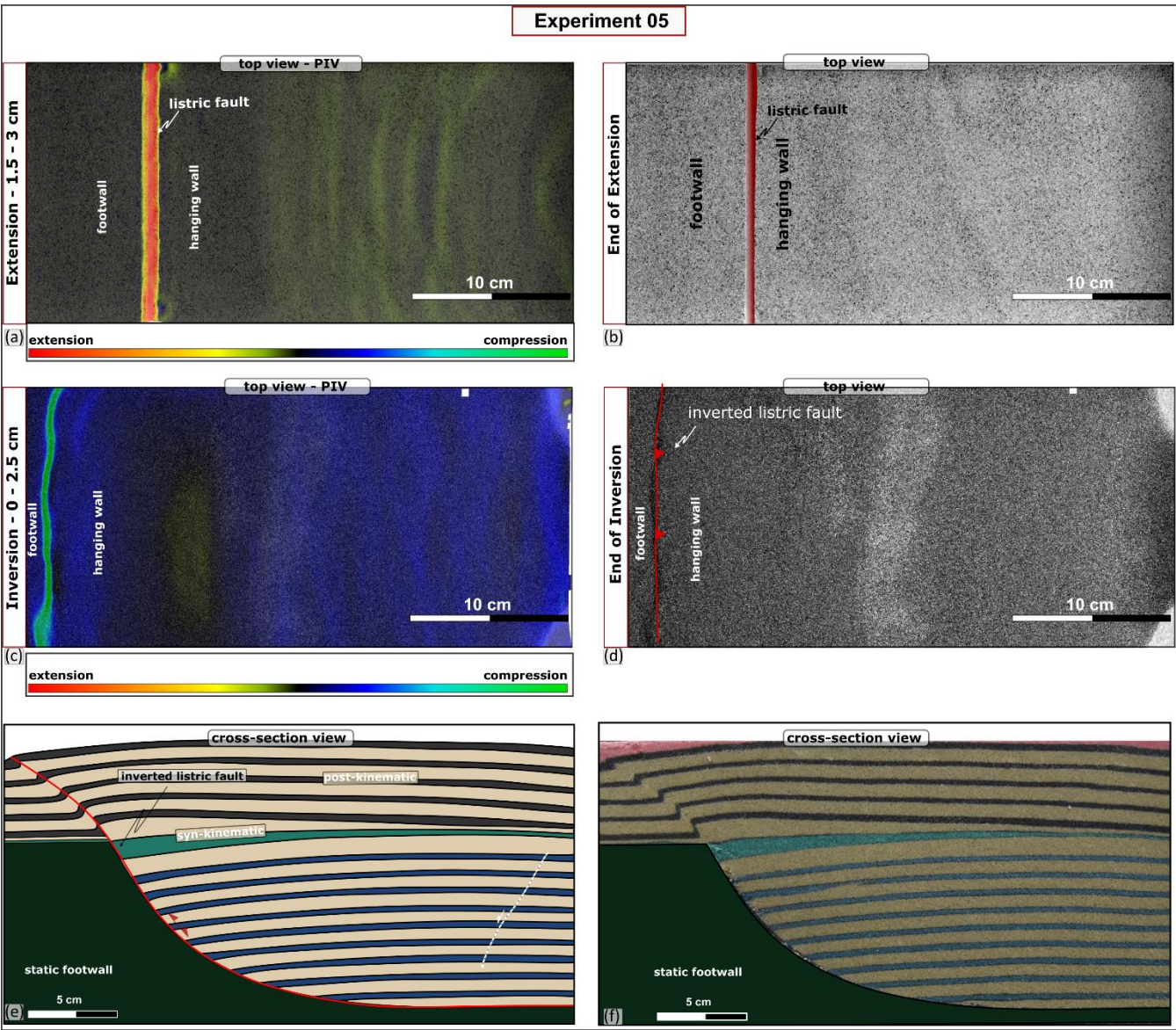


Figure 6. Results of Experiment 4 showing (a-c) the PIV map during syn-sedimentary phase displaying high extensional strain associated with the listric fault (bright red) and areas with (a) diffuse extensional strain (yellow) and (b, c) localised extensional strain in the crestal collapse block. d) Top view of Experiment 4 at the end of extension. e) PIV map during inversion phase displaying high compressional strain above the inverted listric fault (bright green) and areas with diffuse compressional strain (teal). f) Top view of Experiment 4 at the end of inversion (g) Interpreted and (h) uninterpreted cross-section through the experiment.



640 Figure 7. Results of Experiment 5 showing (a) the PIV map during syn-sedimentary phase displaying high extensional strain
associated with the listric fault (bright red) and areas with diffuse to more localised extensional strain (yellow) in the crestal
collapse block. b) Top view of Experiment 5 at the end of extension. c) PIV map during inversion phase displaying high
compressional strain above the inverted listric fault (bright green) and areas with diffuse to more localised compressional strain
(teal). d) Top view of Experiment 5 at the end of inversion. (e) Interpreted and (f) uninterpreted cross-section through the
645 experiment.

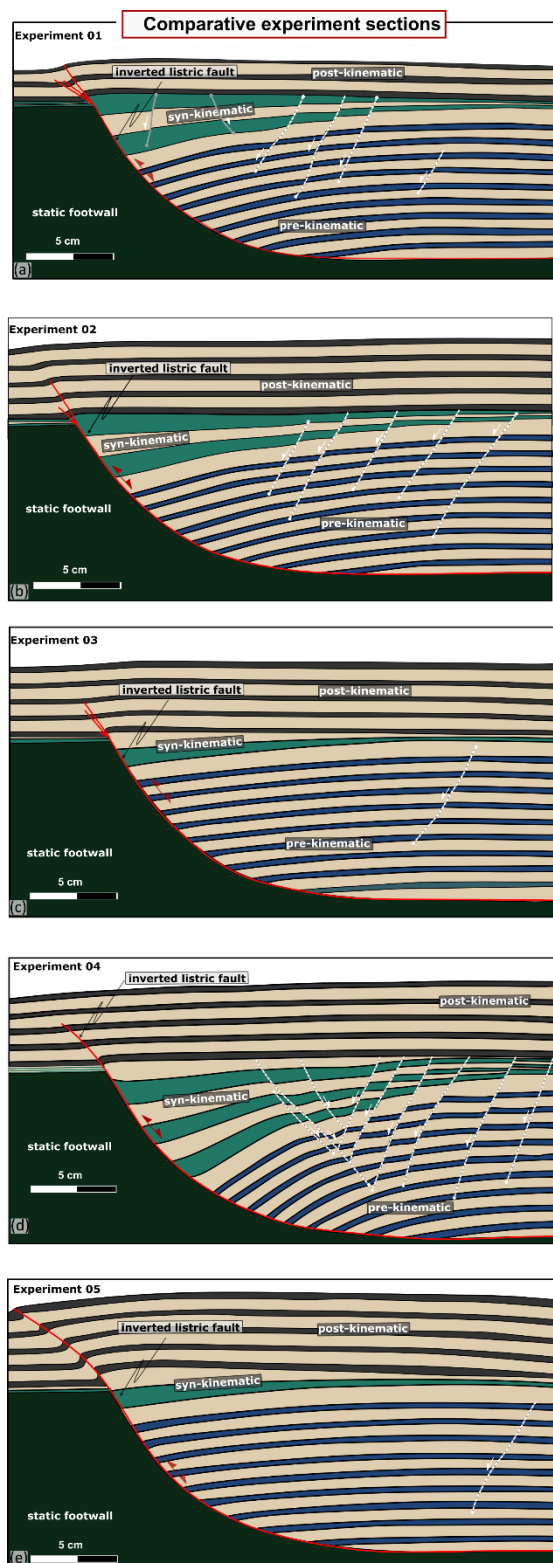


Figure 8. Interpreted cross-section of Experiments 1-5.

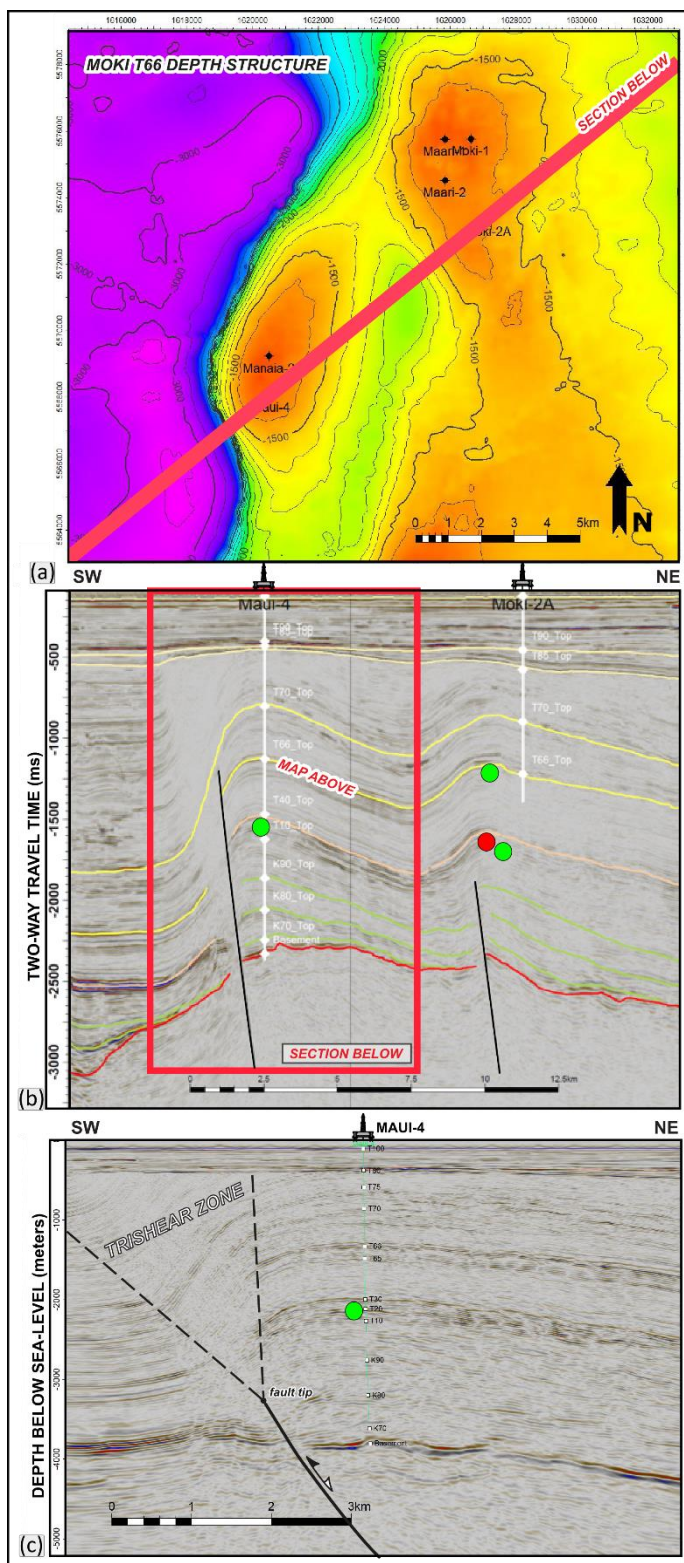


Figure 9. a) Depth structure map of a Miocene stratigraphic horizon in the offshore Taranaki Basin, New Zealand. b) Time-domain seismic reflection example from a 3D data set of the inverted Manaia and Maari productive structures (modified from Wunderlich et al., 2019). Green and red circles stand for oil and gas pay zones, respectively. The Upper Cretaceous strata above the basement (K-70 to K00) is the syn-rift sequence and the overlying Cenozoic (T horizons) is the post-rift succession. These anticlines were formed by Mode II inversion as their inverted post-rift sequence is thicker than the underlying syn-rift part. c) Depth-domain seismic reflection example from a 3D data set of the inverted Manaia anticline showing the tipping master fault and a trishear deformation zone above absorbing the inversion in the post-rift sequence.

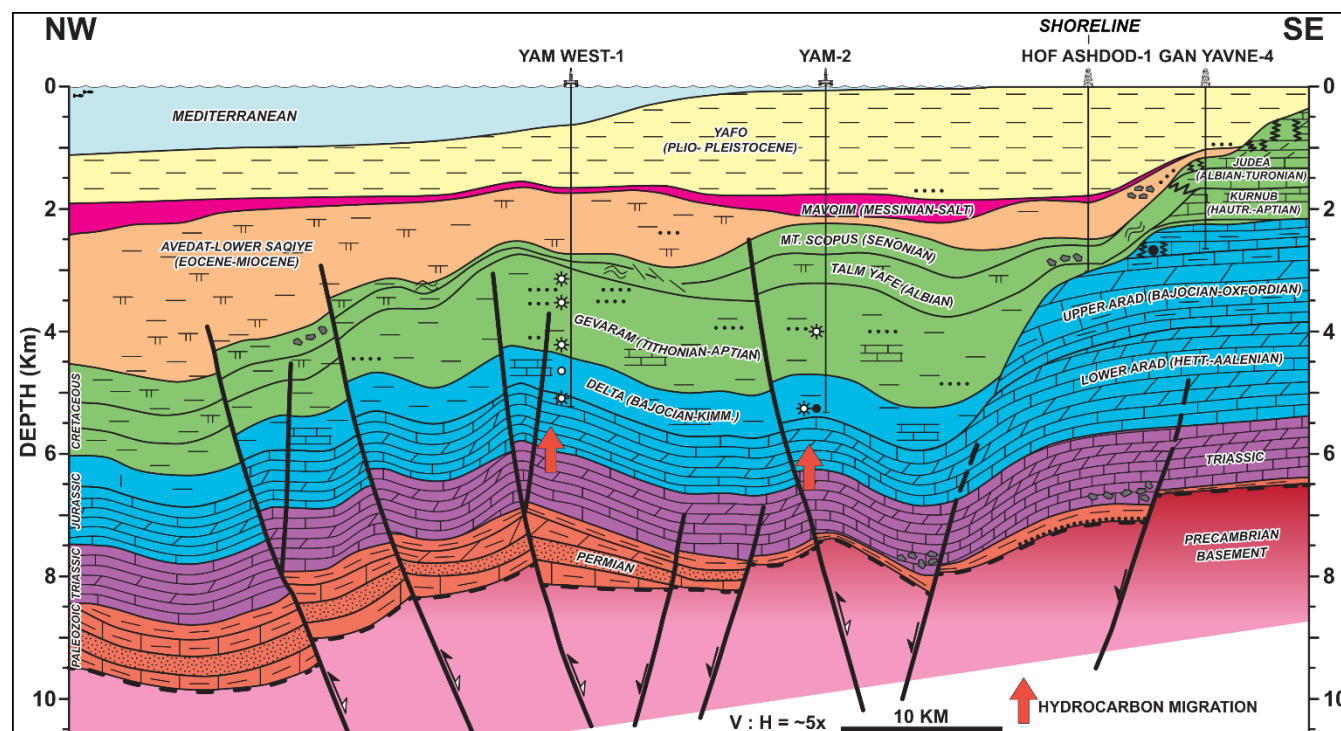


Figure 10. Sub-regional cross-section across the Israeli sector of the Eastern Mediterranean redrafted after (Gardosh et al., 2010). Note that the inversion structures of both Yam West and Yam have a very high post- to syn-rift ratio, around 4-5, qualifying them as Mode II structures sensu Tari et al. (2020).

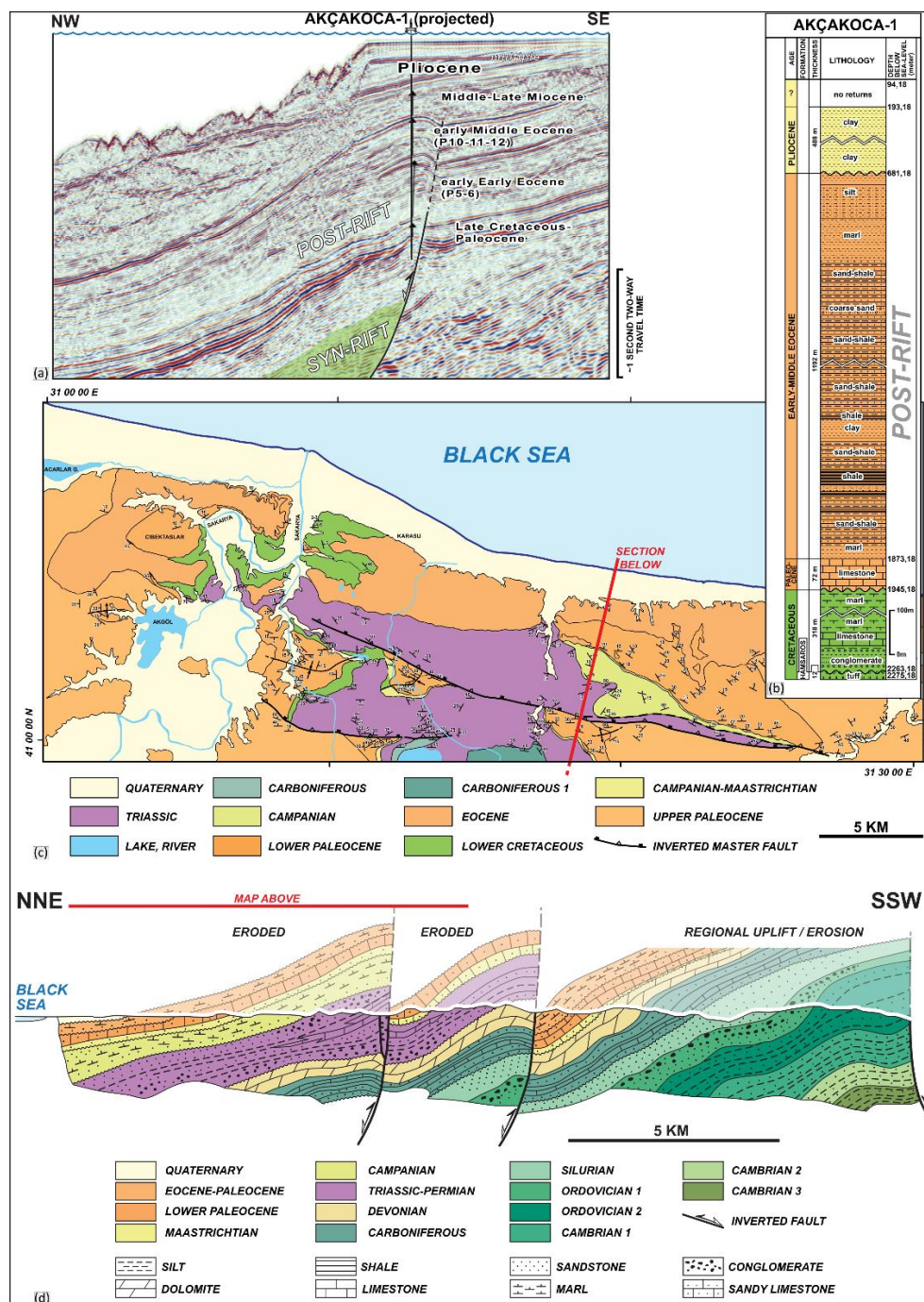


Figure 11. Inversion structures along the Turkish Black Sea coastline in the Akcakoca segment. a) Time-domain 2D reflection seismic line across the Akcakoca gas discovery trend (Korucu et al., 2013). b) Lithostratigraphic summary of the Akcakoca-1 well adapted from (Önal and Demirbag, 2019). c) Geologic map of the coastal area near Sakarya and Akcakoca. d) Geological cross-section adopted from (Aydın et al., 1987) and amended by the interpreted shape of two inversion structures.

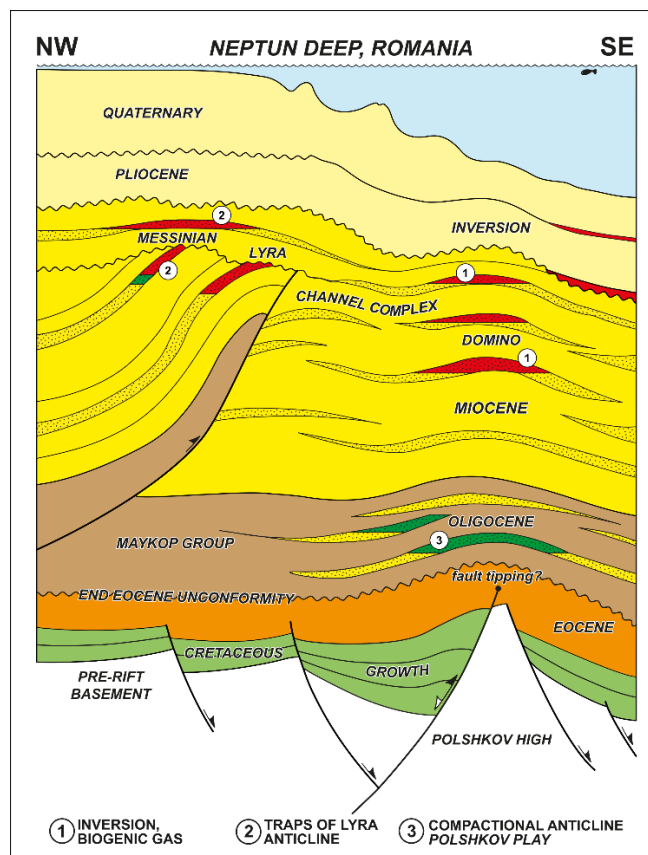


Figure 12. Play concept cartoon of the Domino-1 well drilled in the Romanian sector of the Western Black Sea, modified from (Tari and Simmons, 2018). Note the dominance of the unfaulted Paleogene to Neogene post-rift sequence over the underlying Cretaceous syn-rift strata suggesting Mode II positive inversion.